Analysis and Modeling of Super-Regenerative Oscillators With FSCW Signals

Sergio Sancho, *Senior Member, IEEE*, Mabel Pontón, *Member, IEEE*, and Almudena Suárez, *Fellow, IEEE*

***Abstract*— Active transponders based on super-regenerative oscillators (SROs) have the advantages of a high gain, low consumption, and a compact implementation. They rely on a switched oscillator excited by a low amplitude frequency-modulated continuous-wave (FMCW) signal, which provides an approximately phase-coherent response. Due to the complexity of their operation mode, involving the start-up transient and a time-varying phase shift, their realistic modeling is demanding. Here, we present an in-depth semianalytical investigation of an SRO transponder excited by a frequency-stepped signal, which includes, for the first time to our knowledge, a thorough analysis of the noise perturbations. The SRO is analyzed with a 2-D envelope-domain formulation, derived from a current function extracted from harmonic balance. As will be shown, the SRO response to the incoming signal can be predicted with two nonlinear functions, corresponding to the amplitude and phase, obtained in a single oscillation interval. We will derive an Ornstein–Uhlenbeck system from which the variance of the SRO amplitude and phase will be determined through a detailed analytical approach. Like the SRO response, the noise behavior can be predicted with functions extracted from a single oscillation pulse, which will relate the noise effects to the unperturbed amplitude and phase at the various oscillation stages. The complete investigation provides insight into the effect of nonlinearity and noise on the detected baseband signal and the estimated distance. It will be applied to an SRO at 2.7 GHz, which has been manufactured and measured.**

***Index Terms*— Active transponder, envelope transient, super-regenerative oscillator (SRO).**

I. Introduction

THE switched injection locked oscillator, first proposed in [1], enables the implementation of a novel type of secondary radar system with ranging and communication capabilities. It is based on a super-regenerative oscillator (SRO) that is switched on and off by a quench signal and responds to the interrogation in an approximately phase-coherent manner [1], [2], [3]. Thus, it avoids the need for synchronization with the reader system. Besides its compact implementation, the SRO has the advantages of low power consumption and high gain, mainly due to the oscillator's exponential start-up transient [2], [4]. Following [1] and [5], other concepts and applications have been proposed [6], [7], [8], [9], [10], including positioning based on multiple backscatter transponders [7] and novel implementations with downmixing capabilities to boost the reception frequency [6], using subharmonic downconversion to increase the SRO operating frequency and bandwidth.

From an analysis viewpoint, previous theoretical derivations [1], [2], [3] have established the operating principles of the SRO, which have been experimentally confirmed in [1], [3], [5], [6], [7], [8], [9], and [10]. However, the demonstrations are based on idealized oscillator models and simplified descriptions of specific circuits, such as the cross-coupled architecture considered in [11]. In the analysis of the SRO transponder presented in [1], the switched oscillator is described as a carrier frequency with a rectangular amplitude modulation. Instead, the envelope of the switched oscillation will exhibit a start-up transient and other dynamic effects, disregarded in previous models. In those models, the phase difference between the oscillation and the input signal is assumed to be a linear function of time. However, the oscillation frequency undergoes instantaneous variations during the transient stage, which will affect the SRO response. Although the simplified analyses offer an insightful description of the transponder's operation, they are generally insufficient for accurately predicting the SRO behavior in realistic scenarios.

In the work [12], we presented a realistic modeling approach for an SRO transponder excited by a frequency-stepped continuous wave (FSCW), intended for ranging applications. The model consisted of a nonlinear phase function $\gamma(t, \omega)$, depending on time and the frequency ω of the received signal. The phase function $\gamma(t, \omega)$ was extracted through a circuit-level envelope-transient simulation of the standalone SRO during a single quench period. Then, the response to an FSCW interrogation signal was obtained by introducing the function $\gamma(t, \omega)$ into the system-level description of the complete transponder, including propagation effects and downward mixing. The use of the function $\gamma(t, \omega)$ avoided the need to simulate the oscillator during the entire time interval required to estimate the distance d to the target. However, the function $\gamma(t, \omega)$ in [12] was purely numerical, preventing any insight into the system operation. Moreover, the prediction of noise effects using that function would be limited to costly Monte Carlo simulations.

This work will extend [12] with an in-depth semianalytical investigation of the SRO transponder, including, for the first time to our knowledge, a thorough analysis of the effect of noise perturbations. The SRO analysis will begin with a 2-D envelope-domain formulation [13], which will be treated in

Received 9 July 2024; revised 25 August 2024; accepted 18 September 2024. Date of publication 10 October 2024; date of current version 7 January 2025. This work was supported by Spanish Ministry of Science and Innovation (MCIN/AEI/10.13039/501100011033) under Grant PID2020-116569RB-C31. *(Corresponding author: Sergio Sancho.)*

The authors are with the Departamento Ingeniería de Comunicaciones, Universidad de Cantabria, ETSIIT, 39005 Santander, Spain (e-mail: sanchosm@unican.es).

Color versions of one or more figures in this article are available at https://doi.org/10.1109/TMTT.2024.3470247.

Digital Object Identifier 10.1109/TMTT.2024.3470247

an original manner to facilitate its application to the SRO transponder. This formulation is derived from a current function extracted through circuit-level harmonic balance (HB), under any required number of harmonic terms, which ensures both accuracy and general applicability. To obtain the response of the SRO transponder at each frequency step of the input signal, we will derive, for the first time, an amplitude function and a phase function, defined in a single oscillation interval. Their semianalytical nature will provide insights that are not possible with the black-box envelope-transient analysis of [12]. This should enhance the understanding of the effects of the quench signal and the received signal on the SRO dynamics. Unlike other nonlinear models, the amplitude and phase functions can accurately model potential pulling and locking phenomena [11].

However, the main advantage of the new formulation is its suitability for the noise analysis of the SRO transponder. To this end, the derivations in [13] will be adapted to the transponder system. We will demonstrate that the noise behavior at each input frequency can be modeled using functions extracted from a single oscillation interval, unlike the case of [13]. We will derive an Ornstein–Uhlenbeck system [14] from which the variance of the SRO amplitude and phase will be determined through a detailed analytical approach, presented here for the first time. Note that the circuit-level envelope-transient simulation would be limited to a costly Monte Carlo analysis, offering no insight. The analytical expressions will relate the noise behavior with the unperturbed amplitude and phase at the various stages of the oscillation pulse. For the first time to our knowledge, the new expressions include the oscillator transient and particularize to the results of the well-known works [15], [16] when reaching the periodic steady state. The analysis will aid in understanding how noise perturbations affect the detected baseband signal and the estimated distance. It will be illustrated through its application to an SRO at 2.7 GHz, which has been manufactured and measured.

The article is organized as follows. Section II will demonstrate the possibility to describe the SRO with a phase function, extracted in a single quench interval. Section III will present the semianalytical formulation from which the amplitude and phase functions will be derived. Section IV describes the amplitude and noise analysis. Finally, Section V presents the experimental results.

II. Translation of the Sensor System Dynamics to a Single Quench Interval

A. Operating Principle of the SRO Transponder

The schematic of the SRO transponder system is shown in Fig. 1. The base station transmits a linear stepped-frequency-modulated signal

$$v_{\mathrm{RF}}(t) = V_{\mathrm{RF}} \cos \theta_{\mathrm{RF}}(t) \tag{1}$$

where the instantaneous frequency $\dot{\theta}_{\mathrm{RF}}(t)$ grows in steps $\mu\Delta T$ of time-length ΔT at the sweep rate μ [1]. In an interrogation cycle, it can be expressed as $\dot{\theta}_{\mathrm{RF}}(t) = \omega_k = \omega_{\mathrm{osc}} + \mu(k - N)\Delta T$ for $t \in [k\Delta T, (k+1)\Delta T)$, where ω_{osc} is the free-running frequency of the transponder oscillator, and

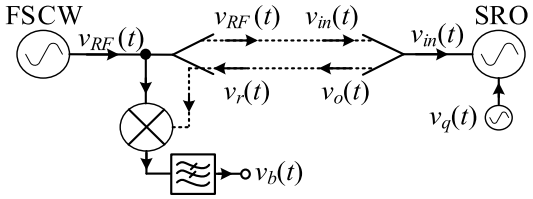

Fig. 1. Block diagram of the SRO transponder system.

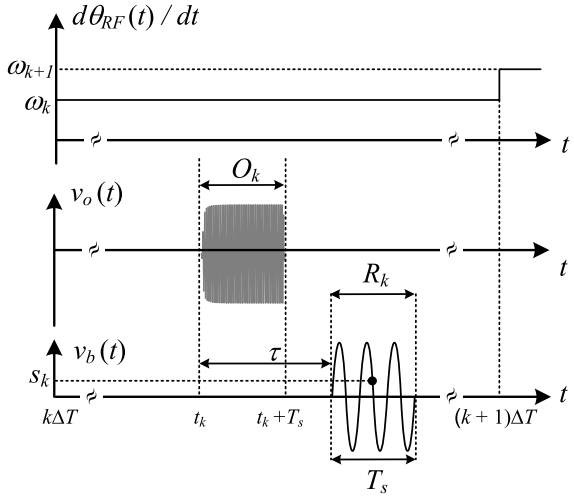

Fig. 2. Schematic showing the time variation of the variables $\dot{\theta}_{\mathrm{RF}}(t)$, $v_o(t)$, and $v_b(t)$ during an interrogation cycle $t \in [k\Delta T, (k+1)\Delta T)$. The time axis is common to the three variables.

$k = 0, \ldots, 2N$ (see Fig. 2). As explained in [1], the overall modulation bandwidth $\Omega = 2N\mu\Delta T$ must be small enough for the instantaneous RF frequency $\dot{\theta}_{\mathrm{RF}}(t)$ to be close to the oscillator free-running frequency ω_{osc}.

The SRO, at a distance d from the transmitter, receives the RF input signal: $v_{\mathrm{in}}(t) = \kappa(d) v_{\mathrm{RF}}(t - \tau) = V_{\mathrm{in}} \cos \theta_{\mathrm{RF}}(t - \tau)$, where $\kappa(d)$ is the attenuation due to the transmission loss, $V_{\mathrm{in}} = \kappa(d) V_{\mathrm{RF}}$ is the attenuated amplitude, and $\tau = d/c$ is the time of flight. On the other hand, the oscillation is switched on and off by a low-frequency T_m-periodic quench voltage signal $v_q(t)$ that modulates the bias voltage. Note that ΔT is larger than T_m. Here, to simplify the analysis, we will choose ΔT to be a multiple of T_m, setting $\Delta T = qT_m$, $q \in Z^+$. Because of the quench source $v_q(t)$, the SRO oscillates during intervals of time length T_s that repeat periodically with period T_m (see Fig. 2). In the time between these intervals, the SRO does not oscillate, providing $v_o(t) \simeq 0$. The output voltage $v_o(t)$ is sent to the transmitter and then mixed with $v_{\mathrm{RF}}(t)$ (see Fig. 1). The resulting signal is filtered by a low-pass filter to obtain the baseband component

$$v_b(t) = (v_r(t) v_{\mathrm{RF}}(t)) * h(t) \tag{2}$$

where $v_r(t) = \kappa(d) v_o(t - \tau)$, $h(t)$ is the impulse response of the filter, and $*$ is the convolution operator. Next, the baseband signal $v_b(t)$ is processed in the following way. Let us consider the interval $[k\Delta T, (k+1)\Delta T]$ corresponding to the kth frequency step. Inside this interval, there are q equivalent subintervals, where $v_b(t) \neq 0$. For each kth frequency step, we will select only one of these intervals R_k denoted as reception subinterval, to take the sample s_k at the receiver (see Fig. 2). Each R_k is associated with an SRO oscillation interval $O_k = [t_k, t_k + T_s]$. Note that at $t = t_k$, the quench signal $v_q(t)$ triggers the oscillation. The reception interval R_k is delayed

from O_k by the time of flight τ, fulfilling $R_k = [t_k + \tau, t_k + T_s + \tau]$. The starting point of each oscillation interval O_k can be expressed as $t_k = k\Delta T + t_0$, where $t_0 + \tau$ is the starting time of the first reception interval R_0. The baseband signal $v_b(t)$ is sampled in R_k obtaining

$$s_k = v_b(t_k + \nu + \tau) \tag{3}$$

where $\nu \in (0, T_s)$. The set of samples is obtained by repeating this procedure for the reception intervals R_k for $k = 0, \ldots, 2N$. The method to estimate the distance d between the transmitter and the SRO from the set of samples $\{s_k\}$ will be presented in Section II-B. In that section, the possibility to model the SRO transponder behavior from the simulation of just one interval for each RF input frequency will be demonstrated.

B. Envelope-Transient Description of the System Dynamics in Each Oscillation Interval O_k

The frequencies $\omega_k \in [\omega_{\text{osc}} - \Omega/2, \omega_{\text{osc}} + \Omega/2]$ and ω_{osc} are, in general, much higher than $\omega_m = 2\pi/T_m$. In the following, only the fundamental-frequency component of the SRO output signal $v_o(t)$ will be considered due to the oscillator output-filtering effects. However, as shown in Section III, the circuit-level analysis will be carried out with NH harmonics. The SRO output signal $v_o(t)$ is

$$v_o(t_k + \xi) \simeq A_k(\xi)\cos\big(\omega_k\xi + \theta_{\text{in},k} + \phi_k(\xi)\big) \tag{4}$$

where $\xi \in [0, T_s]$ is a time variable that extends to the length of the oscillation interval and $\theta_{\text{in},k} = \theta_{\text{RF}}(t_k - \tau)$ is the instantaneous phase of the SRO input at the beginning of O_k. The variables $A_k(\xi)$ and $\phi_k(\xi)$ are the time-varying amplitude and phase of the SRO output voltage at the fundamental frequency in O_k. The fundamental frequency in (4) has been set to ω_k to facilitate the comparison with $v_{\text{RF}}(t)$. Without loss of generality, the time origin can be chosen so that t_0 is a multiple of T_m. Then, the quench signal in O_k satisfies

$$v_q(t_k + \xi) = v_q(\xi) \quad \forall k \tag{5}$$

where the condition $k\Delta T = kqT_m$ has been applied. The RF input at the SRO in O_k is

$$\begin{aligned} v_{\text{in}}(t_k + \xi) &= V_{\text{in}}\cos\theta_{\text{RF}}(t_k + \xi - \tau) \\ &= V_{\text{in}}\cos\left(\omega_k\xi + \theta_{\text{RF}}(t_k) - \omega_k\tau\right) \end{aligned} \tag{6}$$

where we have applied

$$\theta_{\text{in},k} = \theta_{\text{RF}}(t_k) - \omega_k\tau \tag{7}$$

where it has been assumed that the start time of the first oscillation interval O_0 fulfills $t_0 > \tau$. The signals entering the mixer in (2) during the reception interval R_k are

$$\begin{aligned} v_{\text{RF}}(t_k + \xi + \tau) &= V_{\text{RF}}\cos(\omega_k(\xi + \tau) + \theta_{\text{RF}}(t_k)) \\ v_r(t_k + \xi + \tau) &= \kappa(d)A_k(\xi)\cos\big(\omega_k\xi + \theta_{\text{in},k} + \phi_k(\xi)\big). \end{aligned} \tag{8}$$

For the expressions (8) to be valid, the two signals must correspond to the same step of the RF frequency ω_k. This is equivalent to $O_k, R_k \subset [k\Delta T, (k+1)\Delta T]$, implying that $t_k + T_s + \tau < (k+1)\Delta T$. Introducing expressions (8) in (2), the baseband signal in R_k can be approached as

$$v_b(t_k + \xi + \tau) \simeq \frac{1}{2}V_{\text{in}}A_k(\xi)\cos(2\omega_k\tau - \phi_k(\xi)) \tag{9}$$

where it has been assumed that the low-pass filter removes the higher-order frequency components of the mixer output. Next, in each R_k, the signal $v_b(t_k + \xi + \tau)$ is sampled at $\xi = \nu \in (0, T_s)$, which provides the following set of samples (3):

$$s_k = \frac{1}{2}V_{\text{in}}A_k(\nu)\cos(2\omega_k\tau - \phi_k(\nu)) \tag{10}$$

for $k = 0, \ldots, 2N$. In this work, we will make use of the functions $A_k(\xi)$ and $\phi_k(\xi)$ to obtain a realistic model of the SRO transponder. These functions are determined by the initial conditions at the kth oscillation interval. The method to calculate these functions from the simulation of the SRO in the short time interval $\xi \in [0, T_s]$ will be provided in Section III. This will avoid simulating the whole time interval $t \in [0, t_k)$, which will significantly reduce the computational cost and the accumulation of numerical errors.

To illustrate the usage of the new functions, they will be initially particularized to the previous idealized model [1]. This model assumes that the SRO output voltage in O_k has the form

$$v_o(t_k + \xi) = A(\xi)\cos\big(\omega_{\text{osc}}\xi + \theta_{\text{in},k} + \theta_L\big) \tag{11}$$

where $A(\xi)$ is independent of the input frequency ω_k and θ_L is a constant phase shift that is independent of the frequency ω_k of the RF input source. Equating (11) with (4), we obtain the linear function

$$\phi_k(\xi) = (\omega_{\text{osc}} - \omega_k)\xi + \theta_L. \tag{12}$$

Introducing (12) in (9) for $\xi = \nu$ and substituting $\omega_k = \omega_{\text{osc}} + \mu(k - N)\Delta T$, expression (10) becomes

$$s_k = \frac{1}{2}V_{\text{in}}A(\nu)\cos(\omega_b(\tau)k\Delta T + \phi_b(\tau)) \tag{13}$$

which conforms to a periodic sinusoidal signal with frequency

$$\omega_b(\tau) \equiv \mu(2\tau + \nu) \tag{14}$$

and phase

$$\phi_b(\tau) \equiv \omega_b(\tau)\left(\frac{\omega_{\text{osc}}}{\mu} - N\Delta T\right) - \nu\omega_{\text{osc}} + \theta_L. \tag{15}$$

The baseband frequency ω_b resulting in a distance $d = c\tau$ can be detected through the application of the fast Fourier transform (FFT) to the sampled waveform (13). Then, the estimated distance d_e is derived from (14) as

$$d_e = \frac{c}{2}\left(\frac{\omega_b}{\mu} - \nu\right). \tag{16}$$

Note that if the function $\phi_k(\xi)$ agrees with the linear expression (12), the set of samples s_k in (10) conform a sinusoidal signal whose frequency ω_b is given by (14), and therefore, $d_e = d$

$$d_e = \frac{c}{2}\left(\frac{2\pi}{\Delta_L} - \nu\right) = c\tau = d \tag{17}$$

where $\Delta_L = 2\pi/(2\tau + \nu)$. However, we must note that in practice, the frequency dependence of the function $\phi_k(\xi)$ can

be nonlinear, and therefore, $\phi_k(\xi)$ may disagree with the linear expression (12). In addition, the noise sources existing in the SRO will perturb both the amplitude and phase of the output voltage (4), thus distorting the baseband signal (9). Thus, the baseband frequency ω_b obtained from the FFT applied to the set of samples s_k in (10) will be different from the value (14). Consequently, the distance d_e estimated with (16) will differ from the real distance d.

In Sections III and IV, a nonlinear model of the SRO will be derived to analyze both the amplitude and phase functions $A_k(\xi)$, $\phi_k(\xi)$ and the amplitude and phase perturbations produced by the noise sources.

III. Analysis of the SRO Transponder in the Absence of Noise Sources

In principle, envelope transient [17], [18] should be well-suited for the analysis of the SRO transponder due to the existence of two different time scales, associated with the oscillation and the quench signal. However, this circuit-level analysis presents two main drawbacks. On the one hand, its black-box quality prevents understanding the mechanisms by which the external sources influence the SRO's transient dynamics. On the other hand, under the effect of noise sources, the high number of variables involved (NH harmonics for each state variable) will limit the stochastic analysis to brute-force simulations. To perform a realistic and insightful analysis, we will adapt the semianalytical formulation of [13] and [19] to the transponder system. This adapted formulation will be used to obtain the amplitude and phase functions that provide the SRO response to an FSCW in a single oscillation interval.

A. Semianalytical Formulation

We will first consider the HB system that describes the standalone SRO at a given dc value of the quench signal v_q with the RF input source: $v_{\text{in}}(t) = V_{\text{in}} \cos(\omega t + \theta_{\text{in}})$. The voltage at the output node can then be represented as

$$v_o(t) = \sum_{p=-\text{NH}}^{\text{NH}} X_p e^{jp\omega t} \tag{18}$$

where the first harmonic of the series will be expressed as $X_1 = Ae^{j\phi_1}$ with (A, ϕ_1) being constant values. We will make use of the first-harmonic equation resulting from the application of Kirchhoff's current law (KCL) to the oscillator output node

$$I_1(\omega, X) = 0 \tag{19}$$

where I_1 is the first harmonic component of the total current entering the output node and X is the vector containing the harmonic components of the oscillator state variables and input sources. By applying the implicit function theorem [20] to the HB system, we can express $X = X(v_q, A, \phi_1, \omega, V_{\text{in}}, \theta_{\text{in}})$. Thus, (19) can be written as

$$I_1\big(v_q, A, \phi_1, \omega, V_{\text{in}}, \theta_{\text{in}}\big) = 0 \tag{20}$$

where the phase dependence in (20) must preserve the system invariance under a global constant time shift, which is equivalent to

$$I_1\big(v_q, A, \phi_1 + \Delta\alpha, \omega, V_{\text{in}}, \theta_{\text{in}} + \Delta\alpha\big) = 0 \quad \forall \Delta\alpha. \tag{21}$$

Considering (21) and the fact that V_{in} is small, the current function I_1 can be approached by a first-order Taylor series obtaining [22]

$$I_1 = Y\big(v_q, A, \omega\big) A e^{j\phi_1} + B_1 V_{\text{in}} e^{j\theta_{\text{in}}} + B_{-1} V_{\text{in}} e^{j(2\phi_1 - \theta_{\text{in}})}. \tag{22}$$

The coefficients $B_{1,-1}$ are given by $B_1 = (B_r - jB_i)/2$ and $B_{-1} = (B_r + jB_i)/2$, where $B_r \equiv \partial I_1/\partial U^r|_{V_{\text{in}}=0}$ and $B_i \equiv \partial I_1/\partial U^i|_{V_{\text{in}}=0}$, the superscripts r, i in U mean real and imaginary parts, and $U \equiv V_{\text{in}} e^{j\theta_{\text{in}}}$ [22]. Note that the phase dependence in (22) fulfills condition (21). To focus on the phase deviation of the SRO from the input RF source, it is useful to perform in (22) the change of variable $\phi = \phi_1 - \theta_{\text{in}}$. During the SRO performance, the variables $A(t)$ and $\phi(t)$ become time varying by the effect of the quench signal $v_q(t)$. To analyze their dynamics, the frequency dependence in (20) is modified as $\omega \to \omega - js$, where s acts as a time-derivative operator [21]. Since V_{in} is small, the current source I_1 can be approached by a first-order Taylor series about $\omega = \omega_{\text{osc}}$. The use of the quiescent frequency ω_{osc} is enabled by the narrow modulation bandwidth $\Omega \ll \omega_{\text{osc}}$ and the slow-varying nature of the quench frequency ($\omega_m = 2\pi/T_m \ll \omega_{\text{osc}}$). Then, the envelope-domain equation associated with (20) is

$$\begin{aligned} I_1(t) = {} & Y\big(v_q(t), A(t), \omega_{\text{osc}}\big) A(t) \\ & - jY_\omega\big(v_q(t), A(t), \omega_{\text{osc}}\big)\big(\dot{A}(t) + jA(t)\big(\dot{\phi}(t) + \Delta\omega\big)\big) \\ & + I_{\text{in}}\big(v_q, A(t), \phi(t)\big) = 0 \end{aligned} \tag{23}$$

where the admittance function $Y(\eta, A, \omega) = I_1/X_1|_{V_{\text{in}}=0}$ has been introduced, $t \in [0, T_m]$, $\Delta\omega \equiv \omega - \omega_{\text{osc}}$, and the current function I_{in} (depending on V_{in}) models the effect of the RF input source. Note that in (23), we have considered the frequency derivative $Y_\omega(v_q, A, \omega_{\text{osc}}) \equiv \partial Y(v_q, A, \omega_{\text{osc}})/\partial\omega$ [20]. In this analysis, it has been assumed that the quench frequency is low enough to neglect baseband filtering effects on the amplitude and phase dynamics [19]. A full nonlinear dependence is considered in A, which will grow from a very small value to a steady state. The current function I_{in} in (23), accounting for the input signal, has the form

$$I_{\text{in}}(\eta, A, \phi) \equiv B_1 V_{\text{in}} e^{-j\phi} + B_{-1} V_{\text{in}} e^{j\phi} \tag{24}$$

where the coefficients $B_{1,-1}$ depend, in general, on the values of (v_q, A), which will vary during the SRO performance. This dependence is explicitly shown in (23). The nonlinear functions (Y, Y_ω, B_r, B_i) can be easily calculated with circuit-level HB, as explained in Appendix.

The nonlinear system (21) contains two coupled differential equations in the state variables (A, ϕ). Note that when the SRO is introduced in the transponder system, the frequency ω of the RF source varies across the oscillation intervals O_k, which is explicitly indicated with the notation: $A(t, \omega)$ and $\phi(t, \omega)$.

TABLE I
PROCEDURE TO OBTAIN $A(t,\omega)$ AND $\phi(t,\omega)$

1. In system (23), set the initial conditions $A(0,\omega)=\varepsilon$ and $\phi(0,\omega)=\chi$, obtained from (23) by setting $\dot{A}=\dot{\phi}=0$.
2. Solve (23) using time-integration to obtain $A(t,\omega)$ and $\phi(t,\omega)$ in the interval $t\in[0,T_s]$.

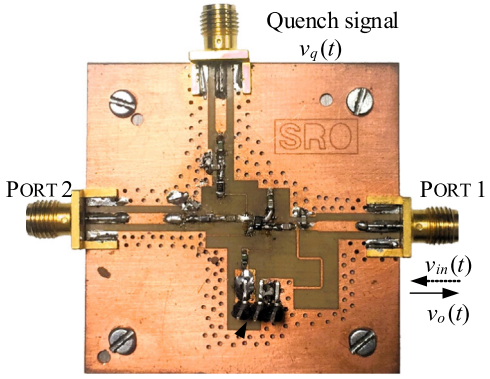

Fig. 3. SRO circuit. The prototype is an FET-based SRO built on Rogers 4003 C substrate ($\varepsilon_r = 3.55$ and $H = 32$ mils). The transistor is an ATF-34143 HEMT. The quench signal $v_q(t)$ is introduced through the gate bias network. Port 1 is used to inject the RF signal $v_{\text{in}}(t)$ and extract the output voltage $v_o(t)$. Port 2 is used to monitor the oscillation signal.

B. Calculation of the Amplitude and Phase Functions $A_k(t)$ and $\phi_k(t)$

As shown in [13], before the quench signal $v_q(t)$ triggers the oscillation, the SRO system will have converged to a periodic solution of small amplitude $A=\varepsilon(V_{\text{in}},\omega)$, with a phase $\phi=\chi(V_{\text{in}},\omega)$, forced by the input RF source, at the frequency ω. This forced solution can be easily obtained by solving (23) for $\dot{A}=\dot{\phi}=0$. Note that the above convergence to the forced solution requires oscillation extinction before the start of each new quench cycle, which is a general condition for the proper operation of any SRO [2]. The dc component, amplitude, and period of the quench signal must be chosen appropriately, which can be achieved through a simple simulation of the SRO in the absence of the RF input. When the oscillation is triggered by $v_q(t)$, the system evolves from this forced solution to the oscillating solution $(A(t,\omega),\phi(t,\omega))$. Thus, the amplitude and phase of the SRO output voltage in the interval O_k are obtained by setting $\omega=\omega_k$ and solving (23) with the initial conditions $A(0,\omega_k)=\varepsilon(V_{\text{in}},\omega_k)$ and $\phi(0,\omega_k)=\chi(V_{\text{in}},\omega_k)$. The integration of (23) provides $A_k(\xi)=A(\xi,\omega_k)$ and $\phi_k(\xi)=\phi(\xi,\omega_k)$, where $\xi\in[0,T_s]$. The complete procedure to calculate the functions $A(t,\omega)$ and $\phi(t,\omega)$ is summarized in Table I.

The analysis method is illustrated through its application to an FET-based oscillator at $\omega_{\text{osc}}=2\pi\cdot 2.76$ GHz shown in Fig. 3. The oscillation is switched on and off with a square voltage signal $v_q(t)$ of period $T_m=1$ μs, introduced through the gate bias network. In the quench cycle $t\in[0,T_m]$, the oscillation is triggered at $t=0$, fulfilling $v_q(0)=v_q^{\text{on}}=-0.7$ V and switched off at $t=T_s$, where $T_s=500$ ns and $v_q(T_s)=v_q^{\text{off}}=-1$ V. The RF amplitude is $V_{\text{in}}=0.2$ mV.

The amplitude and phase components $A(t,\omega)$ and $\phi(t,\omega)$ have been calculated following the procedure of Table I for $(\Delta\omega/2\pi)=-8$ and 8 MHz. They are represented in Fig. 4,

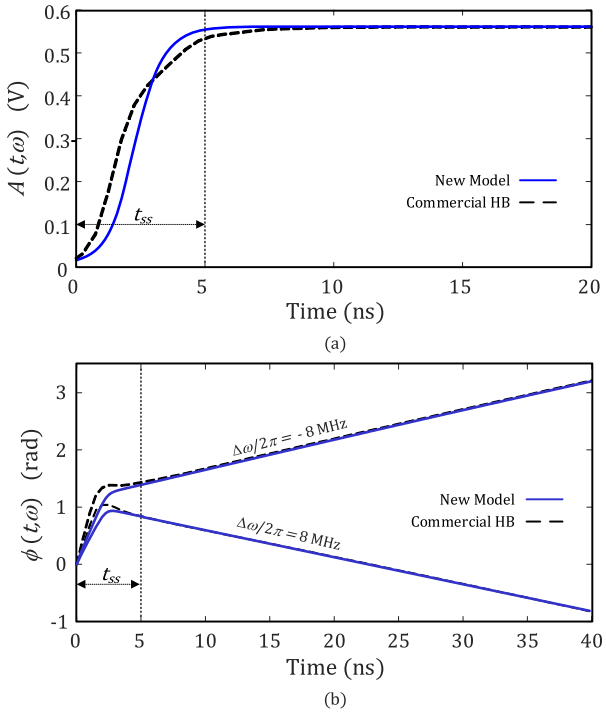

Fig. 4. Simulation of the standalone SRO. The input RF source amplitude and frequency are, respectively, $V_{\text{in}}=0.2$ mV and $\omega=\omega_{\text{osc}}+\Delta\omega$, where $(\Delta\omega/2\pi)=-8$ and 8 MHz. The results of the new model are validated with independent envelop-transient simulations in HB software. (a) Amplitude solution $A(t,\omega)$, which can be approached to be independent of ω. (b) Phase solutions $\phi(t,\omega)$.

where they are validated with independent envelope-transient simulation in commercial HB software (ADS at Keysight). As can be seen, since V_{in} is very small and the SRO operates in the nonlinear mode, the oscillation amplitude $A(t,\omega)$ is practically independent of ω in the frequency range considered. It departs from the small value $A(0,\omega)=\varepsilon(V_{\text{in}},w)$ and eventually reaches the steady state, so the interval $t\in[0,T_s]$ can be divided into transient and steady-state subintervals. For the two frequencies, $\Delta\omega/2\pi=-8$ and 8 MHz, the trajectory reaches the steady state at $t=t_{\text{ss}}\simeq 5$ ns after a transient of rapid growth in $\phi(t,\omega)$ [see Fig. 4(b)]. For $t>t_{\text{ss}}$, the phase $\phi(t,\omega)$ increases or decreases monotonically, depending on the sign of $\Delta\omega/2\pi$. This is because, as demonstrated in [20] and [23], the output voltage $v_o(t)$ contains the beat frequency $\omega'_{\text{osc}}-\omega$, where ω'_{osc} is the SRO autonomous frequency, which can be pulled from its free-running value ω_{osc} toward ω [20], [23]. This makes the mean value of the frequency shift to be $\langle\dot{\phi}(t,\omega)\rangle\simeq\omega'_{\text{osc}}-\omega$ for $t\geq t_{\text{ss}}$. The beat frequency decreases for a smaller $\Delta\omega=\omega_{\text{osc}}-\omega$, which reduces the absolute value of the phase slope of the curves shown in Fig. 4(b).

As shown in Fig. 4, there is a good agreement between the circuit-level envelope transient and the semianalytical formulation. In circuit-level envelope transient, all the circuit state variables are integrated from their initial conditions, while the semianalytical formulation considers the fundamental frequency of the voltage at the observation node and its initial condition. However, in the two cases, the dominant initial values are provided by the RF input, properly captured by the semianalytical formulation. On the other hand, as the oscillation amplitude grows, the structural difference between

the two formulations becomes less relevant since SRO tends to the steady-state oscillation, which should be the same for the two formulations. Their convergence is due to the recovery effect of the steady-state oscillation amplitude.

The sampled phase function $\phi(\nu, \omega)$ has been represented in Fig. 5(a) choosing $\nu = T_s/2$. The result provided by the linear analysis (12) and (13) is superimposed, where a suitable phase shift θ_L has been chosen to facility the comparison. Remember that this value does not influence the distance estimated with (16). If the difference $|\omega - \omega_{\text{osc}}|$ is high enough, we will have $\omega'_{\text{osc}} \simeq \omega_{\text{osc}}$ and $\phi(\nu, \omega) \simeq \phi(t_{\text{ss}}, \omega) + (\omega_{\text{osc}} - \omega)(\nu - t_{\text{ss}})$. Thus, the slope $\partial\phi(\nu, \omega)/\partial\omega \simeq -\nu$ will agree with that of the linear analysis provided in (12). However, as shown in Fig. 4(b), the nonlinear function $\phi(t, \omega)$ exhibits a transient subinterval disregarded by the ideal model (12). The function $\phi(t_{\text{ss}}, \omega)$ is frequency-dependent, which will give rise to discrepancies in the value $\phi(\nu, \omega)$ attained by the two models. Note that these discrepancies are well modeled by system (23), which, for $t > t_{\text{ss}}$, provides the same value of $\phi(t, \omega)$ as the envelope-transient simulation in HB software. In addition, as ω approaches ω_{osc}, we observe a nonlinear behavior near the central region of Fig. 5(a). The integration of (23) can capture the frequency pulling, which will be stronger for a higher V_{in} and a smaller difference between ω and ω_{osc}. For small enough $|\omega - \omega_{\text{osc}}|$, the oscillator may even get locked to the input RF source and $\omega'_{\text{osc}} = \omega$. We would have $\dot{\phi}(t, \omega) = 0$, producing the almost flat central zone. This is observed with both circuit-level envelope transient and semianalytical model, which exhibit a good agreement for the reasons explained above. The pulling effects will be relevant if the distance between the transmitter and the SRO transponder decreases under specific operating conditions or if the transmitted power is too high for a given operating distance.

The effect of the nonlinear functions $A(t, \omega)$ and $\phi(t, \omega)$ on the estimated distance can be analyzed by introducing the frequency-dependent function

$$s(\omega) = \frac{1}{2} V_{\text{in}} A(\nu, \omega) \cos(2\omega\tau - \phi(\nu, \omega)). \tag{25}$$

When varying the input frequency as $\omega_k = \omega_{\text{osc}} + \mu(k - N)\Delta T$, expression (25) provides the set of samples in (10), given by $s_k = s(\omega_k)$. To perform a general analysis, independent of the number N of samples, we will consider the function $s(\omega)$ in terms of continuous $\Delta\omega = \omega - \omega_{\text{osc}}$. This function is shown in Fig. 5(b) for $\nu = T_s/2$, where we have taken $\tau = 40$ ns, corresponding to $d = 12$ m. We will consider the frequency distance Δ_{NL} between two consecutive minima of the function $s(\omega)$. Note that Δ_{NL} defines a pseudoperiod of $s(\omega)$ since, in practice, this function will not be fully periodic. The distance d_e can be estimated from the baseband frequency ω_b obtained from the set of samples lying on the frequency interval comprised between both minima. Considering that the time and frequency steps between samples are, respectively, ΔT and $\mu\Delta T$, this frequency can be approached as $\omega_b \simeq 2\pi\mu/\Delta_{\text{NL}}$. To obtain d_e, we replace ω_b in (16). Comparing with the ideal model, the error produced by the nonlinear

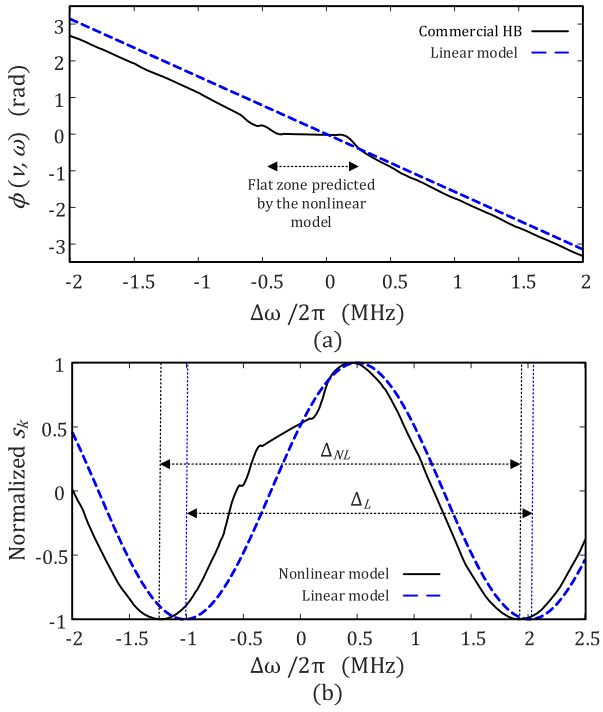

Fig. 5. Simulation of the standalone SRO. (a) Function $\phi(\nu, \omega)$. The linear approach (12) for $\xi = \nu = T_s/2$ has been superimposed, and the size and location of the flat region predicted by the new model have been indicated. (b) Function $s(\omega)$. The values Δ_{NL} and Δ_L correspond to the frequency distance between two consecutive minima of $s(\omega)$.

behavior of $A(t, \omega)$ and $\phi(t, \omega)$ is given by

$$d_e - d \simeq \pi c \left(\frac{1}{\Delta_{\text{NL}}} - \frac{1}{\Delta_L} \right). \tag{26}$$

By choosing the two minima indicated in Fig. 5(b), we have $\Delta_{\text{NL}} > \Delta_L$, and therefore, both approaches produce different values for ω_b. The nonlinear behavior of $\phi(\nu, \omega)$ produces an estimation error $d_e - d \simeq 1.8$ m.

Note that the aim of this work is to provide a technique to detect the deviations of the functions $A(t, \omega)$ and $\phi(t, \omega)$ from the ideal model (12) and (13). For that reason, the simple approach $\omega_b \simeq 2\pi\mu/\Delta_{\text{NL}}$ has been used here to estimate the baseband frequency ω_b. In the literature, there exist more sophisticated techniques, based on the FFT analysis, to extract ω_b from the set of samples s_k [24], [25], [26]. These techniques can be fed with the set of samples provided by (25) using the realistic functions $A(t, \omega_k)$ and $\phi(t, \omega_k)$.

For a given transmitted power, the input-signal amplitude V_{in} depends on the distance d and so does the accuracy of the estimated distance d_e. Note that (25) depends on d through V_{in}, both explicitly and implicitly, as it affects $A(\nu, \omega)$ and $\phi(\nu, \omega)$, which are calculated from (23). The pulling effects will be smaller for a larger d (smaller V_{in}) and will eventually become negligible. On the other hand, the nonlinear transient is inherent to the oscillator circuit, so the impact of the distance d may be relatively small. However, this should be analyzed on a one-by-one basis.

In the case of a frequency-modulated continuous-wave (FMCW) signal, the change in the input frequency is continuous, so some aspects of the analysis will be different. As in the FSCW case, we take one sample in one oscillation interval

every certain number of intervals, so the system analysis can be limited to the sampled ones. It will also be sufficient to consider the input signal at the beginning of the analyzed oscillation intervals. However, with an FMCW signal, the input frequency varies linearly over time, following a ramp-like pattern. This variation must be considered in the integration of the SRO equations and in the calculation of the baseband signal v_b. The detailed analysis of the FMCW case is beyond the scope of this initial work.

IV. Analysis of the Influence of the Noise Sources on the Behavior of the SRO Transponder

In the presence of the SRO noise sources, both the amplitude and phase variables in each oscillation interval O_k get perturbed as

$$\begin{aligned} A_k(t) &= A(t,\omega_k) + \Delta A_k(t) \\ \phi_k(t) &= \phi(t,\omega_k) + \psi_k(t) \end{aligned} \tag{27}$$

where $t \in [0, T_s]$ and $(\Delta A_k(t), \psi_k(t))$ are the components of the amplitude and phase perturbations. Following a derivation analogous to (4)–(10), the samples s_k are given by

$$\begin{aligned} s_k = \frac{V_{\text{in}}}{2}&(A(\nu,\omega_k) + \Delta A_k(\nu)) \\ &\times \cos(2\omega_k\tau - \phi(\nu,\omega_k) + \psi_k(\nu)). \end{aligned} \tag{28}$$

Thus, the detection of the frequency ω_b from the set of samples $\{s_k\}_{k=0}^{2N}$ is altered by the set of random vectors $M = \{z_k(\nu)\}_{k=0}^{2N}$, where $z_k(t) \equiv (\Delta A_k(t), \psi_k(t))^t$. To model the effect of the SRO noise sources, a single current source is placed at the output node, which is fit through a noise analysis of the standalone oscillator. This single source should provide the same noise spectrum obtained with all the existing noise sources [27]. This noise source will be expressed in the same frequency basis as the output voltage in (18)

$$i_n(t) = \text{Re}\left\{I_n(t)e^{j(\omega t + \theta_{\text{in}})}\right\} \tag{29}$$

where the real and imaginary parts of the phasor $I_n(t)$ are stochastic processes. As stated, this current source is introduced at the oscillator output node. Consequently, the envelope domain (23) becomes

$$\begin{aligned} I_1(t) = &Y\left(v_q, A_p, \omega_{\text{osc}}\right)A_p \\ &- jY_\omega\left(v_q, A_p, \omega_{\text{osc}}\right)\left(\dot{A}_p + jA_p\left(\dot{\phi}_p + \Delta\omega\right)\right) \\ &+ I_{\text{in}}\left(v_q, A_p, \phi_p\right) + I_n(t)e^{-j\phi_p} = 0. \end{aligned} \tag{30}$$

The perturbed state variables in (30) are $A_p(t) = A(t,\omega) + \Delta A(t)$ and $\phi_p(t) = \phi(t,\omega) + \psi(t)$, where $A(t,\omega)$ and $\phi(t,\omega)$ are the amplitude and phase functions obtained through the procedure of Table I and $(\Delta A, \psi)$ are the amplitude and phase perturbations. Note that $\Delta A_k(t)$ and $\psi_k(t)$ agree with the perturbation components $\Delta A(t)$ and $\psi(t)$ provided by system (30) for $\omega = \omega_k$. To better understand the transient dynamics, it will be useful to translate equation (30) of the standalone SRO from the complex plane $\mathbb{C}$ to $\Re^2$ using the natural isomorphism $\widehat{u + jv} = (u, v)^t$. This provides

$$\begin{aligned} \hat{I}_1(t) = &a_0A_p + a_1\dot{A}_p + \tilde{a}_1A_p\left(\dot{\phi}_p + \Delta\omega\right) + \hat{I}_{\text{in}} + R\left(-\phi_p\right)\hat{I}_n \\ &= 0 \end{aligned} \tag{31}$$

where $a_0 \equiv \hat{Y}(v_q, A_p, \omega_{\text{osc}})$, $a_1 \equiv -\widehat{jY}_\omega(v_q, A_p, \omega_{\text{osc}})$, $\tilde{a}_1 \equiv \hat{Y}_\omega(v_q, A_p, \omega_{\text{osc}})$, and $R(\phi) \in \text{SO}(2)$ is the rotation matrix of angle ϕ. The advantage of formulating (30) as in (31) is that the components of vector $\hat{I}_1(t)$ in a time-varying orthogonal basis $\{a_1, \tilde{a}_1\}$ provide the amplitude and phase equations. These two equations are directly obtained by making $a_1 \cdot \hat{I}_1(t) = 0$, and $\tilde{a}_1 \cdot \hat{I}_1(t) = 0$, where $\cdot$ means the dot product. The two products provide the following system of Langevin equations:

$$\begin{pmatrix} \dot{A}_p \\ \dot{\phi}_p \end{pmatrix} = g\left(v_q, A_p\right) + h\left(v_q, A_p\right)\left(\hat{I}_{\text{in}} + R\left(-\phi_p\right)\hat{I}_n\right) \tag{32}$$

where $t \in [0, T_s]$ and

$$\begin{aligned} g\left(v_q, A_p\right) &= -\frac{1}{|a_1|^2}\begin{pmatrix} A_p a_1 \cdot a_0 \\ \tilde{a}_1 \cdot a_0 \end{pmatrix} - \begin{pmatrix} 0 \\ \Delta\omega \end{pmatrix} \\ h\left(v_q, A_p\right) &= -\frac{1}{|a_1|^2}\begin{pmatrix} a_1^t \\ \tilde{a}_1^t/A_p \end{pmatrix} \end{aligned} \tag{33}$$

where the superscript t means transposition. Nonlinear system (32) contains two coupled stochastic differential equations in the state variables (A_p, ϕ_p). Note that for a given quench signal $v_q(t)$, the two functions $g(v_q, A_p)$ and $h(v_q, A_p)$ are fully determined by the amplitude variable A_p, whereas the influence on the phase variable ϕ_p is provided by the terms $\hat{I}_{\text{in}}$ and $R(-\phi_p)$. The term $g(v_q, A_p) \in \Re^2$ accounts for the oscillator dynamics. In turn, the influence of the input RF signal and the noise sources depends on the 2×2 matrix $h(v_q, A_p)$. Since the SRO oscillates for a short time T_s, the effect of the low-frequency colored noise sources can be discarded [28]. Thus, the components of the vector $\hat{I}_n(t)$ can be assumed to be white noise sources. These components will fulfill

$$\left\langle \hat{I}_n(t)\hat{I}_n(s)^t \right\rangle = \Gamma\delta(t-s)\begin{pmatrix} 1 & 0 \\ 0 & 1 \end{pmatrix} \tag{34}$$

where $\Gamma \in \Re$, $\delta(t)$ is Dirac's delta and $\langle \hat{I}_n(t) \rangle = 0, \forall t$. To set the initial conditions of (32), we must consider the following. As explained in Section III-B, before the oscillation is triggered, the solution of (32) is nonoscillating and forced by the input RF source, with amplitude $\varepsilon(V_{\text{in}}, \omega)$ and phase $\chi(V_{\text{in}}, \omega)$. Let us consider now the complex stochastic process $X_1^p(t) = A_p(t)e^{j\phi_p(t)}$. Since the forced solution is stable, $X_1^p(0)$ is a normally distributed complex random variable whose probability density function is concentrated in a small disk about $\langle X_1^p(0) \rangle = \varepsilon(V_{\text{in}}, \omega)e^{j\chi(V_{\text{in}},\omega)}$. Due to the small value of $\varepsilon(V_{\text{in}}, \omega)$, this disk can include the origin point in the complex plane, providing a great phase uncertainty in $X_1^p(0)$. The influence of $X_1^p(0)$ is illustrated by considering 10^3 realizations of $X_1^p(t)$ and simulating system (32) during an oscillation interval. We have used the same rectangular quench signal as in the case analyzed in Fig. 4, with $\Delta\omega/2\pi = -6$ MHz and $V_{\text{in}} = 0.2$ mV. The results are shown in Fig. 6(a).

Due to the presence of the RF source, the realization of $X_1^p(t)$ remains close to the unperturbed trajectory $X_1(t) = A(t,\omega)e^{j\phi(t,\omega)}$, superimposed in the same figure. Consequently, the phase uncertainty of $X_1^p(0)$ is significantly reduced in $X_1^p(t)$ for $t > 0$, and the influence of the variance of $X_1^p(0)$ on $X_1^p(t)$ is negligible in comparison with the influence of the

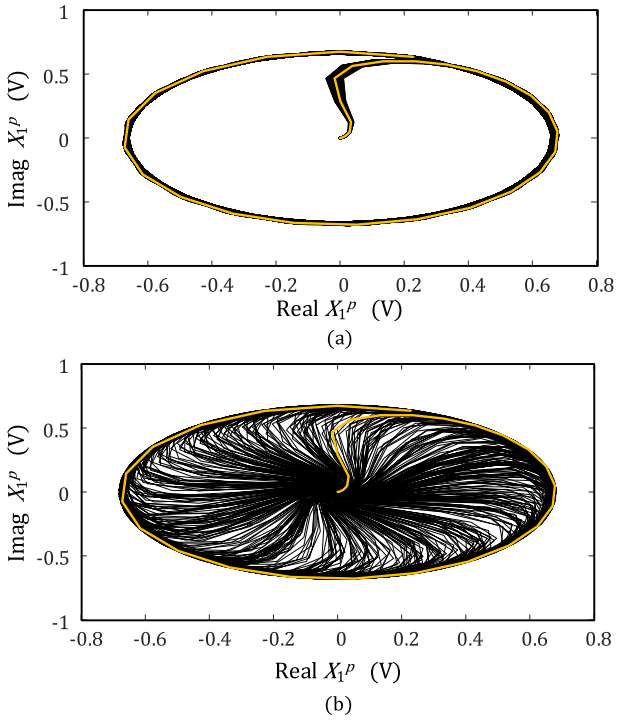

Fig. 6. Time evolution of the perturbed phasor $X_1^p(t)$ in the complex plane. (a) Under the influence of the RF source, the realizations of $X_1^p(t)$ remain close to the unperturbed trajectory $X_1(t)$ (shown in orange). (b) In the absence of the RF source, the uncertainty of the initial phase of $X_1^p(0)$ is transferred to the whole oscillation interval.

noise sources acting along the transient. We have compared the results with those obtained in the absence of the RF source ($V_{\text{in}} = 0$) under the same initial conditions. This second analysis is shown in Fig. 6(b). When removing the RF source, the uncertainty of the initial phase of $X_1^p(0)$ is transferred to the whole oscillation interval. In fact, for proper performance of the SRO transponder, the RF input signal must remove the phase uncertainty accumulated during the nonoscillating interval, as in the example of Fig. 6(a). In this case, the impact of the variance of $X_1^p(0)$ can be neglected. It is possible to consider the initial conditions of (32) to be the deterministic values $A_p(0) = \varepsilon(V_{\text{in}}, \omega)$ and $\phi_p(0) = \chi(V_{\text{in}}, \omega)$ in consistency with [1], [3], and [29].

Considering the small amplitude of the noise sources, system (33) can be linearized about the unperturbed solution $(A(t,\omega), \phi(t,\omega))$. Neglecting quadratic terms in the perturbation components, we obtain the following linear time-variant (LTV) system:

$$\dot{z} = \big(g_A(t)\begin{pmatrix}1 & 0\end{pmatrix} + B(t)\big)z + H(t)\hat{I}_n(t) \tag{35}$$

where $z(t) \equiv (\Delta A(t), \psi(t))^t$, $t \in [0, T_s]$ and

$$\begin{aligned} g_A(t) &\equiv \frac{\partial g\big(v_q, A(t,\omega)\big)}{\partial A} \\ B(t) &\equiv \left.\frac{\partial\big(h\big(v_q, A\big)\hat{I}_{\text{in}}(t)\big)}{\partial(A,\phi)}\right|_{\substack{A=A(t,\omega)\\ \phi=\phi(t,\omega)}} \\ H(t) &\equiv h\big(v_q, A(t,\omega)\big)R(-\phi(t,\omega)). \end{aligned} \tag{36}$$

From (34), $\hat{I}_n(t)dt$ is a 2-D Wiener process, and (35) is an Ornstein–Uhlenbeck system with time-varying coefficients [30]. Following the analysis of Fig. 6, the initial conditions of (35) can be approached to be $z(0) \simeq 0$, and applying the LTV-system theory [22], system (35) can be solved in terms of its fundamental matrix as

$$z(t) = \int_0^t \Phi(t,u)H(u)\hat{I}_n(u)du \tag{37}$$

where $\Phi(t_1,t_2) = P(t_1)P(t_2)^{-1}$ is the state transition matrix and $P(t)$ is the fundamental matrix, which fulfills

$$\dot{P}(t) = \big(g_A(t)\begin{pmatrix}1 & 0\end{pmatrix} + B(t)\big)P(t) \tag{38}$$

where $P(0) = I$. Thus, to obtain $P(t)$, we should integrate the above linear system considering the columns of the identity matrix as initial conditions. The first two moments of the vector random process $z(t)$ can be derived from (37). On the one hand, since $\langle \hat{I}_n(t)\rangle = 0, \forall t$, we have $\langle z(t)\rangle = 0$ for $t \in [0, T_s]$. On the other hand

$$\begin{aligned} &C(t,\omega) \\ &\equiv \big\langle z(t)z(t)^t\big\rangle \\ &= \int_0^t\int_0^t \Phi(t,u_1)H(u_1)\big\langle \hat{I}_n(u_1)\hat{I}_n(u_2)^t\big\rangle H(u_2)^t\Phi(t,u_2)^t du_1 du_2 \\ &= \Gamma\int_0^t \Phi(t,u)H(u)H(u)^t\Phi(t,u)^t du \\ &= \Gamma\int_0^t \frac{\Phi(t,u)\Phi(t,u)^t}{|a_1(u)|^2}du \end{aligned} \tag{39}$$

where $t \in [0, T_s]$ and the double integrand in (39) has been simplified using (34). The matrix $H(u)$ is given by (36), where $R(\phi)$ vanishes due to its orthogonality. Note that the matrix $C(t,\omega)$ depends on the RF frequency ω through the unperturbed components $A(t,\omega)$ and $\phi(t,\omega)$ used in the calculation of the transition matrix $\Phi(t_1,t_2)$. The procedure to calculate the covariance matrix $C(t,\omega)$ is summarized in Table II.

TABLE II
PROCEDURE TO OBTAIN $C(t,\omega)$

1. Obtain the unperturbed solution components $A(t,\omega)$ and $\phi(t,\omega)$ following the procedure of Table I.
2. Use the components $A(t,\omega)$ and $\phi(t,\omega)$ to calculate the functions $g_A(t)$, $B(t)$ and $H(t)$ from (36), for $t \in [0, T_s]$.
3. Solve the homogeneous LTV system (38) in $t \in [0, T_s]$ to obtain the fundamental matrix $P(t)$.
4. Introduce the matrix $\Phi(t_1,t_2) = P(t_1)P(t_2)^{-1}$ in (39) to obtain the matrix $C(t,\omega)$ through numerical integration.

Note that the variance components $\langle \Delta A_k(t)^2\rangle$ and $\langle \psi_k(t)^2\rangle$ agree with the elements on the diagonal of $C(t,\omega)$ calculated through the procedure in Table II for $\omega = \omega_k$. As will be shown, the results agree with the computationally costly Monte Carlo simulations. The formulation (39) provides numerical values, but it is also useful to get analytical insight into the dependence of the variances $\langle \Delta A_k(t)^2\rangle$ and $\langle \psi_k(t)^2\rangle$ on the unperturbed variables $A(t,\omega)$ and $\phi(t,\omega)$. In the following, this dependence is first analyzed in the case of a standalone switched oscillator (homogeneous case). The analysis is illustrated in the oscillator studied in Fig. 4, using the

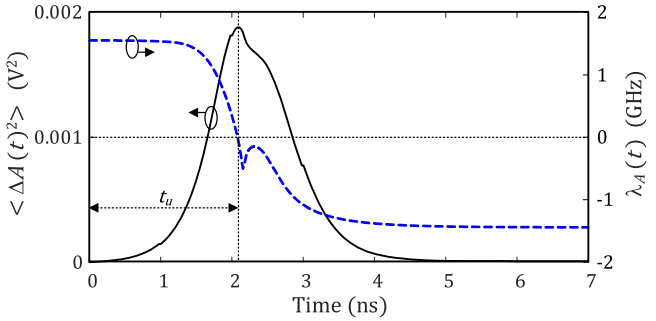

Fig. 7. Stochastic analysis of the free-running SRO. Time-varying variance of the amplitude noise $\Delta A(t)$ in the most significative part of the interval $t \in [0, T_s]$. The amplitude pole $\lambda_A(t)$, whose sign determines the growth or decrease of this variance, has been superimposed. For $t \in [0, t_u)$, $\lambda_A(t) > 0$ and the amplitude variance grows. For $t \in (t_u, T_s]$, $\lambda_A(t) < 0$ and the unperturbed amplitude decreases, becoming negligible in the steady-state interval $t \in [t_{ss}, T_s]$, where the unperturbed amplitude $V_o(t)$ settles (see Fig. 8).

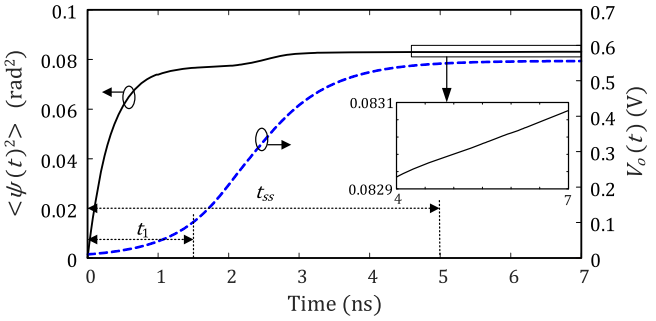

Fig. 8. Stochastic analysis of the free-running SRO. Time-varying variance of the phase noise $\psi(t)$ in the most significative part of the interval $t \in [0, T_s]$. The unperturbed amplitude $V_o(t)$ has been superimposed. For $t \in [0, t_1]$, $V_o(t)$ is small, and in agreement with (48), the variance undergoes fast growth. For $t \in [t_1, t_{ss}]$, the amplitude noise burst is integrated by (39), producing a step on the phase variance. Finally, for $t \in [t_{ss}, T_s]$, the unperturbed amplitude settles about $V_o = V_{ss}$, and the phase variance grows linearly with time, in agreement with (51).

same rectangular quench signal. The results are then extended to the SRO (non-homogeneous case), where an independent validation with a Monte Carlo simulation will be performed. Finally, we address the sampled baseband signal.

A. Homogeneous Case

The homogeneous case corresponds to $V_{in} = 0$ and $\omega = \omega_{osc}$. System (35) becomes

$$\begin{aligned} \Delta\dot{A} &= g_{A,1}(t)\Delta A + H_1(t)\cdot\hat{I}_n \quad \text{(a)} \\ \dot{\psi} &= g_{A,2}(t)\Delta A + H_2(t)\cdot\hat{I}_n \quad \text{(b)} \end{aligned} \tag{40}$$

where $g_{A,i}(t)$ and $H_i(t)$ for $i = 1, 2$ are the ith component of the vector $g_A(t)$ and the vector composed by the ith row of the matrix $H(t)$, respectively. To get insight, we will make use of the analytical expression of the vectors $H_i(t)$, which regulate the influence of the noise sources on the system dynamics

$$\begin{aligned} H_1(t) &= -\frac{1}{|a_1|^2}R(\phi(t,\omega))a_1 \\ H_2(t) &= -\frac{1}{|a_1|^2 V_o(t)}R(\phi(t,\omega))\tilde{a}_1 \end{aligned} \tag{41}$$

where, to simplify the notation, we have denoted the unperturbed amplitude in this homogeneous case as $V_o(t) \equiv A(t, \omega_{osc})$. As observed in (40), in this homogeneous case, the explicit dependence on $\psi(t)$ vanishes. Consequently, the amplitude (40a) is independent of the phase variable and can be separately analyzed. The variance $\langle\Delta A(t)^2\rangle$ calculated through the procedure of Table II is represented in Fig. 7. To ease the further comparison with the nonhomogeneous case ($V_{in} > 0$), the initial conditions of the unperturbed components have been set to $A(0, \omega_{osc}) = \varepsilon(V_{in}, \omega_{osc})$ and $\phi(0, \omega_{osc}) = \chi(V_{in}, \omega_{osc})$ with $V_{in} = 20\ \mu$V. The behavior of $\langle\Delta A(t)^2\rangle$ can be explained in terms of the components of the amplitude (40a). In the absence of noise perturbations, $V_o(t)$ fulfills $\dot{V}_o(t) = g_1(V_o(t))$, where g_1 is the first component of the vector g. Considering this equation, the coefficient $g_{A,1}(t)$ of (40a) is given by $g_{A,1}(t) = \partial\dot{V}_o(V_o(t))/\partial V_o \equiv \lambda_A(t)$, where $\lambda_A(t)$ will be called the amplitude pole. Using this pole, the solution of (40a) can be expressed as

$$\Delta A(t) = \int_0^t \alpha_A(t,u)H_1(u)\cdot\hat{I}_n(u)du \tag{42}$$

where $\alpha_A(t,s) = \exp\int_s^t \lambda_A(u)du$. As already stated, just before the oscillation is triggered, the system remains in a stable nonoscillating steady-state solution, providing $\langle\Delta A(0)\rangle \simeq \langle\Delta A(0)^2\rangle \simeq 0$. Then, the initial condition $\Delta A(0) \simeq 0$ has been imposed in (42). The time-varying pole $\lambda_A(t)$, which is superimposed in Fig. 7, governs the behavior of the amplitude variance. To see this, let us first derive $\langle\Delta A(t)^2\rangle$ from (42), expressing $H_1(t)$ as in (41) and applying (34)

$$\langle\Delta A(t)^2\rangle = \Gamma\int_0^t \frac{\alpha_A(t,s)^2}{|a_1(s)|^2}ds. \tag{43}$$

Next, using (43), we derive the following rule for the time evolution of $\langle\Delta A(t)^2\rangle$:

$$\begin{aligned} \langle\Delta A(t+\Delta t)^2\rangle &= \alpha_A(t+\Delta t,t)^2\langle\Delta A(t)^2\rangle \\ &\quad + \Gamma\int_t^{t+\Delta t}\frac{\alpha_A(t,s)^2}{|a_1(s)|^2}ds \end{aligned} \tag{44}$$

where $\Delta t \geq 0$. At $t = 0$, the quench source triggers the oscillation by making the dc solution unstable with $\lambda_A(0) > 0$. The unperturbed amplitude $V_o(t)$ grows from this point until it settles at $V_o(t \geq t_{ss}) \simeq V_{ss} = 0.55$ V, where $t_{ss} \simeq 5$ ns, as shown in Fig. 8. Due to the system continuity, we will have $\lambda_A(t) > 0$ in a time interval $t \in [0, t_u)$, where $t_u < t_{ss}$ (see Fig. 7). Then, for $t, t + \Delta t \in [0, t_u)$, we have $\alpha_A(t + \Delta t, t)^2 > 1$, and consequently, $\langle\Delta A(t + \Delta t)^2\rangle > \langle\Delta A(t)^2\rangle$, in agreement with the behavior shown in Fig. 7. From the definition of $\alpha_A(t,s)$, given by $\alpha_A(t,s) = \exp\int_s^t \lambda_A(u)du$, the maximum variance attained is proportional to the maximum value of $\lambda_A(t)$ in $[0, t_u)$.

For $t \in (t_u, T_s]$, by setting $t = t_u$ in (44), we observe two different contributions to $\langle\Delta A(t_u + \Delta t)^2\rangle$. On the one hand, the amplitude pole fulfills $\lambda_A(t) < 0$, producing $\alpha_A(t_u + \Delta t, t_u)^2 < 1$. Consequently, the first term of (44) decreases with time. On the other hand, the integral term of (44) grows monotonically with Δt. This growth is bounded since, as shown in Fig. 8, for $t \simeq t_{ss}$, the unperturbed amplitude settles to $V_o = V_{ss}$. Considering a square quench signal, the

vectors $a_o(V_o(t))$ and $a_1(V_o(t))$ in O_k are fully determined by $V_o(t)$, so they will also settle. Therefore, the amplitude pole becomes constant

$$\lambda_A(t_{ss}) = \frac{\partial \dot{V}_o(V_o(t_{ss}))}{\partial V_o} = g_{A,1}(t_{ss}) \simeq V_{ss}\frac{a_1^{ss}\cdot a_{0V}^{ss}}{\left|a_1^{ss}\right|^2} \tag{45}$$

where $a_1^{ss} \equiv a_1(V_{ss})$ and $a_{0V}^{ss} \equiv \partial a_0(V_{ss})/\partial V$. Since the dynamics of $V_o(t)$ is governed by a first-order equation, its convergence to the steady-state interval is asymptotic, fulfilling $\lambda_A(t_{ss}+\Delta t) \simeq \lambda_A(t_{ss}) < 0$. Therefore, $\alpha_A(t_{ss}+\Delta t, t_{ss}) \to 0$ for $\Delta t \to \infty$. Then, using (44) and (45), we have

$$\lim_{\Delta t\to\infty}\left\langle \Delta A(t_u+\Delta t)^2\right\rangle = \frac{\Gamma}{2V_{ss}a_1^{ss}\cdot a_{0V}^{ss}} \tag{46}$$

which is in agreement with Fig. 7, where, for $t \in (t_u, T_s]$, the variance of the amplitude perturbation decreases to a small value (46). This is because of the recovery effect of the steady-state oscillation amplitude.

The variance $\langle\psi(t)^2\rangle$ calculated numerically is represented in Fig. 8. To analyze its behavior, the phase perturbation is derived from (40b) as

$$\psi(t) = \psi(0) + \int_0^t g_{A,2}(t)\Delta A(s)ds + \int_0^t H_2(t)\cdot \hat{I}_n(s)ds. \tag{47}$$

From (41), $|H_2(t)| \propto 1/V_o(t)$, and therefore, this term is dominant in the phase equation (47) for small values of $V_o(t)$ Then, there exists a time interval $[0, t_1]$, where the phase variance can be approached from (47) as

$$\langle\psi(t)^2\rangle \simeq \langle\psi(0)^2\rangle + \Gamma\int_0^t |H_2(s)|^2 ds = \langle\psi(0)^2\rangle + \Gamma\int_0^t \frac{ds}{V_o(s)^2|a_1(V_o(s))|^2} \tag{48}$$

where $t \in [0, t_1]$ and $|H_2(s)|^2$ has been derived using (41). Expression (48) predicts a fast-growing phase variance for small $V_o(t)$, in agreement with Fig. 8. Note that the procedure of Table II considers the initial variance $\langle\psi(0)^2\rangle = 0$ since, as stated before, in the nonhomogeneous case ($V_{in} > 0$), the presence of the RF source should remove the impact of this initial uncertainty. For $t > t_1$, the amplitude $V_o(t)$ is big enough to give rise to a noticeable reduction in this growth rate. In fact, in the subinterval $t \in [t_1, t_{ss}]$, the burst of the amplitude perturbation shown in Fig. 7 is translated to the phase by the coefficient $g_{A,2}(t)$, producing a step in the phase variance when integrated in (39). As already seen, in the steady-state interval, the amplitude variance decreases to a small value (46). Consequently, we can approach $\Delta\dot{A} \simeq 0$ in (40), which leads to

$$\dot{\psi}(t) \simeq k_\psi \cdot \hat{I}_n(t) \tag{49}$$

where $t \in [t_{ss}, T_s]$ and

$$k_\psi = \frac{g_{A,2}(t_{ss})}{g_{A,1}(t_{ss})}H_1(t_{ss}) + H_2(t_{ss}). \tag{50}$$

Note that k_ψ is a constant vector coefficient that can be analytically obtained in terms of the vector functions $a_0(V_{ss})$, $a_1(V_{ss})$, using (33) and (36). Applying (34) and neglecting the second-order derivatives in a_0 and a_1, we obtain the following expression for the phase variance:

$$\left\langle\psi(t)^2\right\rangle \simeq \left\langle\psi(t_{ss})^2\right\rangle + \frac{\Gamma\left|a_{0V}^{ss}\right|^2}{V_{ss}^2\left(a_1^{ss}\cdot a_{0V}^{ss}\right)^2}(t-t_{ss}) \tag{51}$$

where $t \in [t_{ss}, T_s]$. Expression (51) predicts that in the steady-state interval, the phase variance grows linearly with time (zoomed-in view in Fig. 8). This result is consistent with the analyses [15], [31], [32] of the phase-noise variance of the periodic steady-state solution of a free-running oscillator in the presence of white noise sources. Note that the investigation presented here extends the analysis of the amplitude and phase variance to the oscillator transient regime. This new analysis includes the steady state as a limit case.

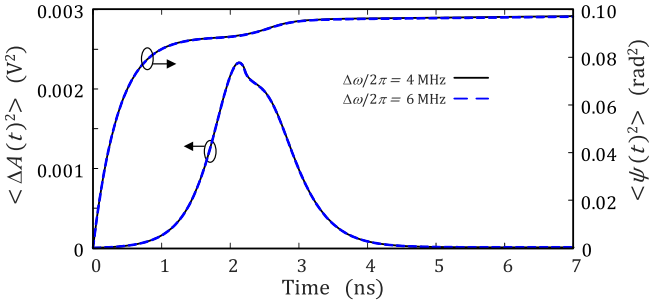

Fig. 9. Stochastic analysis of the injected SRO for $\omega = \omega_{osc} + \Delta\omega$, where $(\Delta\omega/2\pi) = 4$ and 6 MHz. Time-varying variance of the amplitude and phase perturbation components $\Delta A(t,\omega)$ and $\psi(t,\omega)$. The qualitative behavior of both components during the transient subinterval is like the free-running case, as shown in Figs. 7 and 8.

B. Nonhomogeneous Case

Here, we will analyze the time-varying amplitude and phase variances in the presence of the RF input signal ($V_{in} > 0$). To illustrate the influence of the frequency ω of the RF input source, the cases $\Delta\omega/2\pi = 4$ and 6 MHz have been considered. As seen in Fig. 9, during the transient to the limit cycle ($t \le 5$ ns), the behavior of $\langle\Delta A(t)^2\rangle$ and $\langle\psi(t)^2\rangle$ is similar to that of the homogeneous case (see Figs. 7 and 8). Due to the large value of $\langle\Delta A(t)^2\rangle$ during the transient, we should avoid setting the sampling time ν in the transient interval. However, as $A(t,\omega)$ approaches the steady-state value V_{ss}, $\langle\Delta A(t)^2\rangle$ becomes negligible. As in the homogeneous case, this is because of the recovery effect of the steady-state oscillation under amplitude perturbations.

The behavior of $\langle\psi(t)^2\rangle$ after the oscillation has settled (see Fig. 10) can be predicted from the unperturbed phase $\phi(t,\omega)$. The result has been validated with a Monte Carlo simulation. As in the homogeneous case, for $A(t,\omega) \simeq V_{ss}$, the amplitude variance is negligible, and we can approach $\dot{A} \simeq 0$ in (32). Then, for $t \in [t_{ss}, T_s]$, (32) becomes a first-order ordinary differential equation (ODE) in the phase variable. Thus, it can be rewritten as $\dot{\phi}_p \simeq F(\phi_p, \hat{I}_n)$. Using the decomposition $\phi_p(t) = \phi(t,\omega) + \psi(t)$, we can linearize this equation about the unperturbed state ($\hat{I}_n = 0$), obtaining

$$\dot{\psi} \simeq \frac{\partial F(\phi(t,\omega),0)}{\partial\phi}\psi + \frac{\partial F(\phi(t,\omega),0)}{\partial n}\hat{I}_n = \lambda_\psi(t)\psi + k_\psi\cdot\hat{I}_n. \tag{52}$$

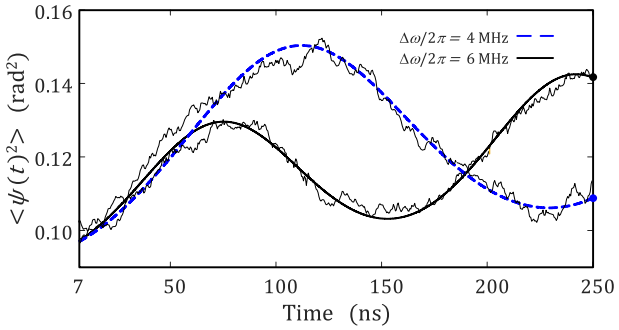

Fig. 10. Stochastic analysis of the injected SRO for $\omega = \omega_{\text{osc}} + \Delta\omega$, where $(\Delta\omega/2\pi) = 4$ and 6 MHz. Time-varying variance of the phase perturbation component $\psi(t)$ in the most significant part of the steady-state subinterval. The RF amplitude is $V_{\text{in}} = 0.2$ mV. The values $\langle\psi(v)^2\rangle$, where $v = T_s/2 = 250$ ns, are marked with points. The results of the new model have been independently validated with a Monte Carlo simulation with 10^3 realizations (superimposed).

Note that the expression of the vector coefficient k_ψ is given in (50). The term $\lambda_\psi(t)$ in (52) will be called the phase pole. By considering that $\dot{\phi}(t,\omega) = F(\phi(t,\omega),0)$, the phase pole $\lambda_\psi(t)$ can be obtained from the unperturbed phase function $\phi(t,\omega)$ as

$$\lambda_\psi(t) = \frac{\partial\dot{\phi}(t,\omega)}{\partial\phi(t,\omega)} = \frac{\ddot{\phi}(t,\omega)}{\dot{\phi}(t,\omega)} \tag{53}$$

where $t \in [t_{\text{ss}}, T_s]$. Since the time dependence is provided by $\phi(t,\omega)$, $\lambda_\psi(t)$ varies periodically at the beat frequency $\omega'_{\text{osc}} - \omega$. Note that for $V_{\text{in}} = 0$, at the steady-state ($\dot{A} \simeq 0$) system, (23) produces $\dot{\phi}(t,\omega) = -\Delta\omega$, and therefore, according to (53), $\lambda_\psi(t) = 0$. The phase variance in the steady state can be analyzed by first solving $\psi(t,\omega)$ from the LTV equation (52) and then obtaining $\langle\psi(t)^2\rangle$ as

$$\langle\psi(t)^2\rangle \simeq \alpha_\psi(t,t_{\text{ss}})^2\langle\psi(t_{\text{ss}})^2\rangle + \frac{\Gamma|a_{0\text{V}}^{\text{ss}}|^2}{V_{\text{ss}}^2\left(a_1^{\text{ss}}\cdot a_{0\text{V}}^{\text{ss}}\right)^2}\int_{t_{\text{ss}}}^{t}\alpha_\psi(t,s)^2 ds \tag{54}$$

where $t \in [t_{\text{ss}}, T_s]$ and $\alpha_\psi(t,s) = \exp\int_s^t \lambda_\psi(u)du$. The term $\alpha_\psi(t,t_{\text{ss}})^2\langle\psi(t_{\text{ss}})^2\rangle$ in (54) and the phase pole $\lambda_\psi(t)$ are represented in Fig. 11, for two values of the RF input frequency. In the two cases, $\lambda_\psi(t)$ oscillates periodically at the beat frequency $\omega'_{\text{osc}} - \omega$ taking positive and negative values. Hence, as shown in Fig. 11(a), the function $\alpha_\psi(t,t_{\text{ss}})^2$ modulates the time-varying phase variance and is responsible for its oscillating nature. As deduced from the definition of $\alpha_\psi(t,s)$, given by $\alpha_\psi(t,s) = \exp\int_s^t \lambda_\psi(u)du$, the maxima and minima of $\alpha_\psi(t,t_{\text{ss}})^2$ agree with the zero crossings of $\lambda_\psi(t)$ with negative and positive slopes, respectively. The second term in (54) is a monotonically growing component, whose growth rate is modulated by $\alpha_\psi(t,t_{\text{ss}})$. The function $\alpha_\psi(t,t_{\text{ss}})$, which can be obtained from the unperturbed phase $\phi(t,\omega)$, determines the qualitative behavior of the variance $\langle\psi(t)^2\rangle$ for $t > t_{\text{ss}}$ with no need to solve (39).

Note that as already stated, in the homogeneous case, $\lambda_\psi(t) = 0$ for $t > t_{\text{ss}}$. In this case, $\alpha_\psi(t,t_{\text{ss}}) = 1$, and (54) agrees with the linearly growing phase variance (51).

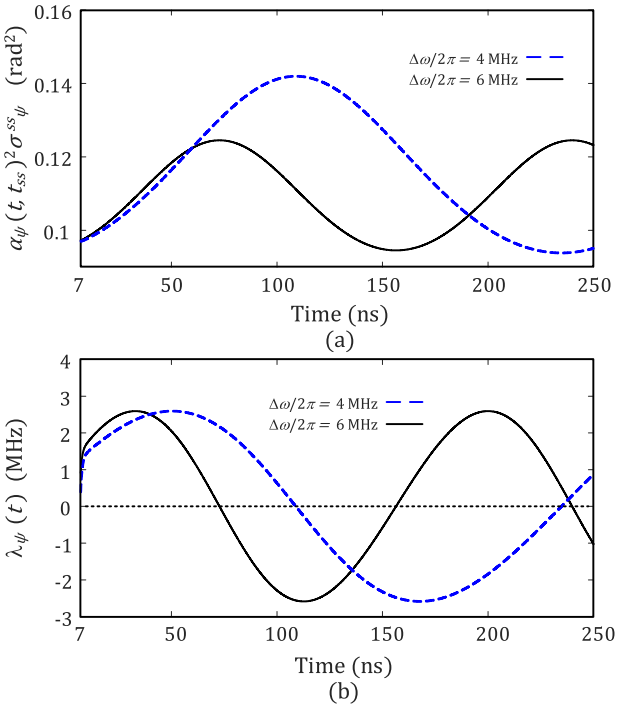

Fig. 11. Stochastic analysis of the injected SRO for $\omega = \omega_{\text{osc}} + \Delta\omega$, where $(\Delta\omega/2\pi) = 4$ and 6 MHz. Prediction of the behavior of $\langle\psi(v)^2\rangle$ during the steady-state interval shown in Fig. 10. (a) Oscillatory behavior of $\langle\psi(v)^2\rangle$ is well predicted by the term $\alpha_\psi(t,t_{\text{ss}})^2\sigma^{\text{ss}}_\psi$. (b) Maxima and minima of $\langle\psi(v)^2\rangle$ agree with the zero crossings of $\lambda_\psi(t)$ with negative and positive slopes, respectively.

When the RF frequency ω gets close to ω_{osc} or the amplitude V_{in} increases, the oscillator may get locked to the input RF signal. In that case, as stated in Section III-B, the signal $\phi(t,\omega)$, converges to a constant value, where the SRO instantaneous frequency becomes $\omega + \dot{\phi}(t,\omega) = \omega$. Since $\phi(t,\omega)$ obeys the first-order system $\dot{\phi}(t,\omega) = F(\phi(t,\omega),0)$, its convergence must be asymptotic. Then, according to (53), the phase pole fulfills $\lambda_\psi(t) < 0$, and expression (54) becomes

$$\lim_{t\to\infty}\langle\psi(t)^2\rangle = \frac{\Gamma|a_{0\text{V}}^{\text{ss}}|^2}{2V_{\text{ss}}^2\left(a_1^{\text{ss}}\cdot a_{0\text{V}}^{\text{ss}}\right)^2} \tag{55}$$

showing that in the locked case, the phase variance decreases down to small value (55).

Under a given transmitted power, the input amplitude V_{in} decreases as the distance d increases, resulting in greater uncertainty in the estimated distance d_e. If the noise becomes too significant relative to the received signal, the oscillator's phase will have difficulty tracking the phase of the RF input. This is because, as seen in system (30), the noise sources act as additional inputs that make tracking more difficult. Because the sampling is carried out, while the oscillation is in a steady state, only the phase noise will be relevant. In an approximate manner, the degradation as noise increases can be quantified using the following figure of merit:

$$S_{\text{in}}/N = 10\log_{10}\frac{V_{\text{in}}^2}{\frac{V_o(t_{\text{ss}})^2}{v}\int_0^v\langle\psi(t)^2\rangle dt}. \tag{56}$$

At $\Delta\omega/2\pi = 4$ MHz, for $V_{\text{in}} = 0.2$ mV ($d = 12$ m) and $V_{\text{in}} = 0.1$ mV ($d = 24$ m), we obtain $S_{\text{in}}/N = -60$ dB and $S_{\text{in}}/N = -65$ dB, respectively.

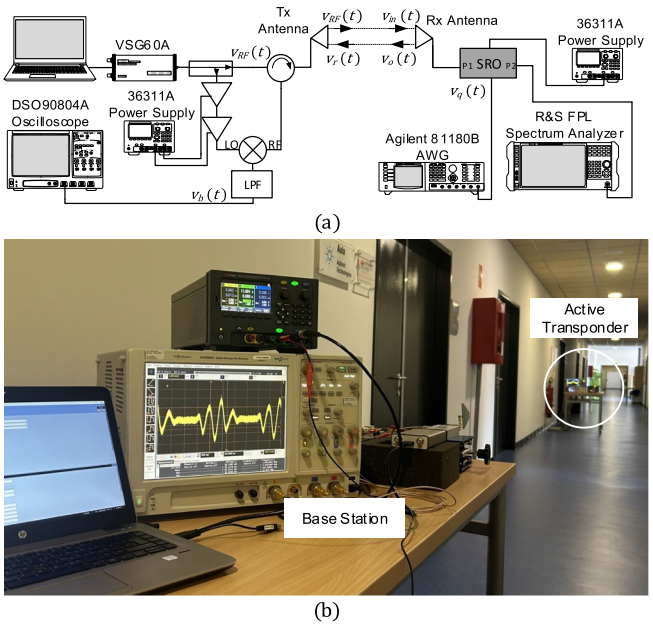

Fig. 12. Test bench. (a) Schematic. (b) Photograph of the implementation for a distance $d = 12$ m.

C. Stochastic Properties of Baseband Sampled Signal

Expression (28) for the perturbed samples s_k can be approached by a first-order Taylor series expansion as

$$s_k \simeq \frac{V_{\text{in}}}{2}(A(\nu,\omega_k)+\Delta A_k(\nu))(\cos(2\omega_k\tau-\phi(\nu,\omega_k)) - \sin(2\omega_k\tau-\phi(\nu,\omega_k))\psi_k(\nu)) \quad (57)$$

where, as shown at the beginning of Section IV, $\langle \Delta A_k(\nu)\rangle = \langle \psi_k(\nu)\rangle = 0$. Let us consider that the samples s_k are obtained in the steady-state interval ($\nu > t_{\text{ss}}$) to avoid the burst of the amplitude process. Then

$$\langle s_k\rangle \simeq \frac{V_{\text{in}}}{2}A(\nu,\omega_k)\cos(2\omega_k\tau-\phi(\nu,\omega_k)) \quad (58)$$

where, considering $\nu > t_{\text{ss}}$, the correlation terms between the amplitude and phase perturbations have been neglected. Using (57) and (58), the second-order central moment of these samples $\sigma_k^2 \equiv \langle (s_k - \langle s_k\rangle)^2\rangle$ can be approached as

$$\sigma_k^2 = \frac{V_{\text{in}}^2}{4}A(\nu,\omega_k)^2\sin^2(2\omega_k\tau-\phi(\nu,\omega_k))\langle\psi_k(\nu)^2\rangle \quad (59)$$

where we have applied that $\langle \Delta A(\nu)^2\rangle \simeq 0$ for $\nu > t_{\text{ss}}$, as previously derived. Expression (59) shows that the moments σ_k^2 are affected both by the unperturbed functions $A(\nu,\omega_k)$, $\phi(\nu,\omega_k)$ and the variance of the phase perturbation $\langle\psi_k(\nu)^2\rangle$. In Section V, expression (59) will be applied to predict the central moments of the noisy samples extracted from the measurements.

V. Measurement Results

The new model has been validated using the test bench shown in Fig. 12. The stepped-frequency-modulated signal $v_{\text{RF}}(t)$ is generated with a Signal Hound VSG60A Vector Signal Generator and transmitted using a PCB log periodic antenna with a gain of 5 dBi. A similar receiving antenna is connected to port 1 of the SRO, and an R&S FPL spectrum analyzer is connected to port 2 to monitor the oscillation.

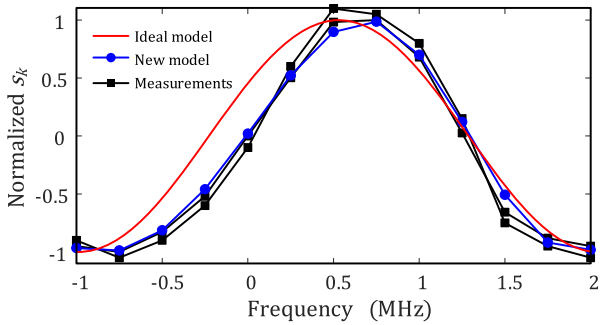

Fig. 13. Normalized sampled baseband signal for $d = 12$ m. Comparison of the simulated results with two sets of measured samples s_k.

The sinusoidal quench signal is generated with an Agilent 8118B Arbitrary Waveform Generator. In the base station, a circulator isolates the transmitted signal $v_{\text{RF}}(t)$ from the received signal $v_r(t)$. A sample of the RF signal is obtained using a 10-dB directional coupler and mixed with the received signal $v_r(t)$ using a Mini-Circuits ZEM-4300+ mixer. Since the RF signal sample has very low power, two Mini-Circuits ZX60-6013E-S+ amplifiers are required to adjust the LO power in the mixer. High-frequency components are filtered at the mixer output with a Mini-Circuits SLP-10.7+ Low Pass Filter. The baseband signal $v_b(t)$ is monitored with an Agilent DSO90804A Digital Oscilloscope. Finally, Keysight E36311A dc power supply sources have been used to bias the amplifiers and the SRO.

To get the set of samples, we have used a stepped frequency-modulated signal with $N = 65$ steps of size $\mu\Delta T/2\pi = 250$ kHz, with time between steps $\Delta T = 1$ μs. The frequency of the square quench signal is $f_m = 1$ MHz, and the length of the oscillation interval is $T_s = 500$ ns. To avoid the undesired pulling effects predicted in the analysis of Fig. 5 for ω close to ω_{osc}, the transmitted power has been reduced to provide an input RF signal of $P_{\text{in}} \simeq -64$ dBm. We have separated the base station and the transponder by a distance of $d = 12$ m. This corresponds to a time delay of $\tau = 40$ ns. By sampling each oscillation interval at $\nu = T_s/2$, we obtain a set of voltage samples s_k conforming a period curve. Each sample s_k has been obtained using the average option in the oscilloscope data acquisition. Fig. 13 shows two sets of samples. Note that by the effect of the phase perturbation, each s_k in (28) is a random variable that will provide different results in each measurement. The samples obtained with the new nonlinear model (25) and the ideal model (12)–(14) have been superimposed in Fig. 13. As can be seen, the new model is able to predict the nonideal behavior of the measured samples. Considering the step frequency $\mu\Delta T/2\pi = 250$ kHz between samples, the application of (26) bounds the distance estimation error to $d_e - d \leq 2$ m.

Next, to validate the noise analysis of Section IV, we have obtained the sequence of second-order central moments of the samples $\sigma_k^2 \equiv \langle (s_k - \langle s_k\rangle)^2\rangle$. In Fig. 14, the values of the components σ_k^2 obtained from the experimental measurements are compared with those obtained from (59). From the moments σ_k^2, we can predict the impact of the noise perturbations at the different frequency steps. This is valuable for FFT-based techniques [24], [25], [26] that, departing from the set of samples s_k, enable the calculation of the estimated distance d_e.

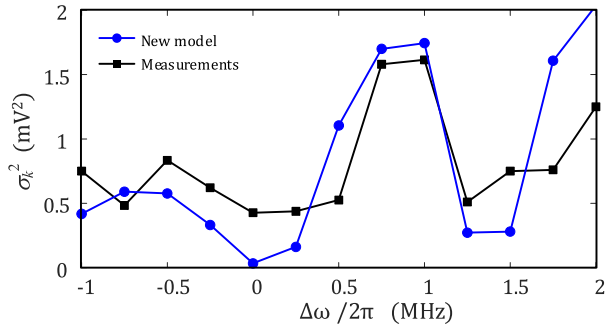

Fig. 14. Second-order central moments $\sigma_k^2 \equiv \langle (s_k - \langle s_k \rangle)^2 \rangle$ for $d = 12$ m. Comparison between the measured values with the predictions of model (59).

With the central moments σ_k^2, it should be possible to obtain the uncertainty in the estimated distance.

The predictions of the new model (see Fig. 14) resemble the measurement results. However, there are discrepancies that we attribute to modeling inaccuracies and tolerances, particularly in the active device. This is supported by the fact that the baseband-signal samples, s_k, obtained with circuit-level envelope transient exhibit similar disagreements with the experimental results, as shown in [12]. In fact, the most reliable validation of the new analysis method is the comparison with circuit-level envelope transient. This is because, only in this comparison, we can be sure that the models of all the circuit components (both active and passive) are identical.

VI. Conclusion

This work has presented an in-depth semianalytical investigation of the SRO transponder excited with a frequency-stepped signal, including an insightful analysis of the effect of noise perturbations. Our study demonstrated that the SRO behavior at each input frequency could be modeled using functions extracted from a single oscillation interval. We described the SRO response to each frequency step using amplitude and phase functions defined in a single oscillation interval. They are obtained from a 2-D envelope-domain formulation, which is developed from a nonlinear current function, extracted from HB. In addition, we derived an Ornstein–Uhlenbeck system to determine the variance of the SRO amplitude and phase perturbations through a detailed analytical approach, presented here for the first time. Unlike costly Monte Carlo analyses, our analytical expressions offer clear insights by relating noise behavior to the unperturbed amplitude and phase during different stages of the oscillation pulse. Extending this analysis to the entire transponder system revealed valuable effects on the detected baseband signal and the estimated distance. To validate our method, it was applied to a 2.7-GHz SRO, which was manufactured and measured. This work enhances the understanding of SRO behavior under noise perturbations, providing practical insights for designing more robust transponder systems.

Appendix
Calculation of the Nonlinear Coefficients

The nonlinear coefficients (Y, Y_ω, B_r, B_i) can be calculated using circuit-level HB, following the procedure described in [19] and summarized here. First, the quench voltage is set to a dc value $v_q = V_q$, and the oscillator is forced with an auxiliary generator (AG) [20], introduced into the oscillator circuit at the output node (see Fig. 15). This AG is composed of a one-tone voltage source of amplitude A, phase 0, and frequency ω_{AG} in series with an ideal filter of admittance $Y_f(\omega) = \delta(\omega - \omega_{\mathrm{AG}})$. The input RF source is set to $v_{\mathrm{in}}(t) = \mathrm{Re}\{U e^{j\omega_{\mathrm{AG}} t}\}$. Consequently, the current entering the AG is a function $I_{\mathrm{AG}}(V_q, A, \omega_{\mathrm{AG}}, U^r, U^i)$ that can be calculated by solving the circuit of Fig. 15 in circuit-level HB. Using this function, we obtain

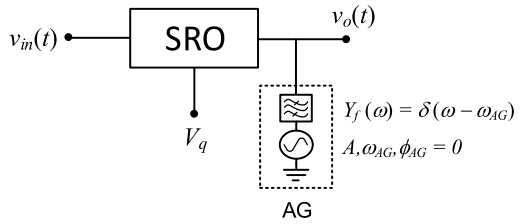

Fig. 15. Schematic of the SRO used for the calculation of the nonlinear functions. The quench voltage is set to a dc value $v_q = V_q$, and the oscillator is forced with an AG [20], introduced into the oscillator circuit at the output node.

$$
\begin{aligned}
Y\left(V_q, A, \omega_{\mathrm{osc}}\right) &= \frac{I_{\mathrm{AG}}\left(V_q, A, \omega_{\mathrm{osc}}, 0, 0\right)}{A} \\
Y_\omega\left(V_q, A, \omega_{\mathrm{osc}}\right) &= \frac{1}{A}\frac{\partial I_{\mathrm{AG}}\left(V_q, A, \omega_{\mathrm{osc}}, 0, 0\right)}{\partial \omega} \\
B_{r,i}\left(V_q, A\right) &= \frac{\partial I_{\mathrm{AG}}\left(V_q, A, \omega_{\mathrm{osc}}, 0, 0\right)}{\partial U^{r,i}}.
\end{aligned} \tag{60}
$$

The functions in (60) are obtained through a double sweep in (V_q, A). At each point of the sweep, the partial derivatives are obtained through the method of finite differences using small increments in ω_{AG} and $U^{r,i}$ about $\omega_{\mathrm{AG}} = \omega_{\mathrm{osc}}$ and $U = 0$, respectively.

References

[1] M. Vossiek and P. Gulden, "The switched injection-locked oscillator: A novel versatile concept for wireless transponder and localization systems," *IEEE Trans. Microw. Theory Techn.*, vol. 56, no. 4, pp. 859–866, Apr. 2008.

[2] P. Pala-Schönwälder, J. Bonet-Dalmau, F. X. Moncunill-Geniz, F. del Águila-López, and R. Giralt-Mas, "A superregenerative QPSK receiver," *IEEE Trans. Circuits Syst. I, Reg. Papers*, vol. 61, no. 1, pp. 258–265, Jan. 2014.

[3] A. Ferchichi, H. Ghaleb, C. Carta, and F. Ellinger, "Analysis and design of 60-GHz switched injection-locked oscillator with up to 38 dB regenerative gain and 3.1 GHz switching rate," in *Proc. IEEE 61st Int. Midwest Symp. Circuits Syst.*, Aug. 2018, pp. 340–343.

[4] F. X. Moncunill-Geniz, J. Bonet-Dalmau, F. Del Aguila-Lopez, I. Demirkol, and P. Pala-Schonwalder, "Super-regenerative receiver for OFDM communication," in *Proc. IEEE Int. Symp. Circuits Syst. (ISCAS)*, Nov. 2022, pp. 1843–1847.

[5] M. V. Thayyil, S. Li, N. Joram, and F. Ellinger, "A K-band SiGe superregenerative amplifier for FMCW radar active reflector applications," *IEEE Microw. Wireless Compon. Lett.*, vol. 28, no. 7, pp. 603–605, Jul. 2018, doi: 10.1109/LMWC.2018.2839063.

[6] L. Hahn, M. Vossiek, and C. Carlowitz, "A low-power, subharmonic super-regenerative receiver toward a massive multichannel FMCW radar close to cut-off frequency," in *IEEE MTT-S Int. Microw. Symp. Dig.*, Jun. 2023, pp. 513–516.

[7] M. Schtz, Y. Dobrev, C. Carlowitz, and M. Vossiek, "Wireless local positioning with SILO-based backscatter transponders for autonomous robot navigation," in *IEEE MTT-S Int. Microw. Symp. Dig.*, Apr. 2018, pp. 1–4, doi: 10.1109/ICMIM.2018.8443524.

[8] L. Hahn, M. Vossiek, and C. Carlowitz, "A subharmonic super-regenerative FMCW radar with improved intermodulation efficiency for applications beyond cut-off frequency," *IEEE Trans. Microw. Theory Techn.*, vol. 72, no. 1, pp. 797–811, Jan. 2024, doi: 10.1109/TMTT.2023.3316305.

[9] M. Schütz, Y. Dobrev, T. Pavlenko, and M. Vossiek, "A secondary surveillance radar with miniaturized transponders for localization of small-sized UAVs in controlled air space," in *Proc. 5th IEEE Int. Workshop Metrology Aerosp.*, Jun. 2018, pp. 107–111.

[10] H. Ghaleb, N. Joram, and F. Ellinger, "A 60-GHz super-regenerative oscillator with 80 dB gain in SiGe BiCMOS for FMCW radar active reflectors," in *Proc. IEEE 22nd Topical Meeting Silicon Monolithic Integr. Circuits RF Syst. (SiRF)*, Jan. 2022, pp. 31–34.

[11] A. Ferschischi, H. Ghaleb, M. Schulz, U. Jörges, C. Carta, and F. Ellinger, "Nonlinear analysis of cross-coupled super-regenerative oscillators," *IEEE Trans. Circuits Syst. I, Reg. Papers*, vol. 68, no. 6, pp. 2368–2381, Jun. 2021.

[12] S. Sancho, M. Ponton, and A. Suarez, "Analysis and modeling of super-regenerative oscillators with FMCW signals," in *IEEE MTT-S Int. Microw. Symp. Dig.*, Jun. 2024, pp. 846–849.

[13] S. Sancho, S. Hernández, and A. Suárez, "Noise analysis of super-regenerative oscillators in linear and nonlinear modes," *IEEE Trans. Microw. Theory Techn.*, vol. 67, no. 12, pp. 4955–4965, Dec. 2019.

[14] C. W. Gardiner, *Handbook of Stochastical Methods*. Cham, Switzerland: Springer, 1997.

[15] F. X. Kaertner, "Analysis of white and $f^{-\alpha}$ noise in oscillators," *Int. J. Circuit. Theory Appl.*, vol. 18, pp. 485–519, Aug. 1990.

[16] A. Demir, "Phase noise in oscillators: DAEs and colored noise sources," *IEEE Trans. Circuits Syst. I, Fundam. Theory Appl.*, vol. 49, no. 12, pp. 170–177, 2002.

[17] E. Ngoya and R. Larcheveque, "Envelop transient analysis: A new method for the transient and steady state analysis of microwave communication circuits and systems," in *IEEE MTT-S Int. Microw. Symp. Dig.*, vol. 3, Jul. 1996, pp. 1365–1368.

[18] N. B. Carvalho, J. C. Pedro, W. Jang, and M. B. Steer, "Simulation of nonlinear RF circuits driven by multi-carrier modulated signals," in *IEEE MTT-S Int. Microw. Symp. Dig.*, Jun. 2005, pp. 801–804.

[19] S. Sancho, A. Suárez, and F. Ramírez, "Two-band model of super-regenerative oscillators," *IEEE Trans. Microw. Theory Techn.*, vol. 72, no. 2, pp. 1018–1029, Feb. 2024, doi: 10.1109/TMTT.2023.3292621.

[20] A. Suarez, *Analysis and Design of Autonomous Microwave Circuits*. Hoboken, NJ, USA: Wiley, 2009.

[21] K. Kurokawa, "Some basic characteristics of broadband negative resistance oscillator circuits," *Bell Syst. Tech. J.*, vol. 48, no. 6, pp. 1937–1955, Jul. 1969.

[22] S. Sancho, F. Ramírez, and A. Suárez, "Stochastic analysis of cycle slips in injection-locked oscillators and analog frequency dividers," *IEEE Trans. Microw. Theory Techn.*, vol. 62, no. 12, pp. 3318–3332, Dec. 2014.

[23] B. Razavi, "A study of injection locking and pulling in oscillators," *IEEE J. Solid-State Circuits*, vol. 39, no. 9, pp. 1415–1424, Sep. 2004.

[24] M. Cerna and A. F. Harvey, *The Fundamentals of FFT-Based Signal Analysis and Measurement*, document 041, 2000.

[25] M. Tabei and M. Ueda, "A method of high-precision frequency detection with FFT," *Electron. Commun. Jpn., Part I*, vol. 71, no. 11, pp. 24–32, Nov. 1988.

[26] Y. Wu and J. P. M. G. Linnartz, "Detection performance improvement of FMCW radar using frequency shift," in *Proc. IEEE SP Symp. Inf. Theory Signal Proces*, May 2011, pp. 1–20.

[27] F. Ramirez, M. Ponton, S. Sancho, and A. Suarez, "Phase-noise analysis of injection-locked oscillators and analog frequency dividers," *IEEE Trans. Microw. Theory Techn.*, vol. 56, no. 2, pp. 393–407, Feb. 2008, doi: 10.1109/TMTT.2007.914375.

[28] S. Hernandez, S. Sancho, and A. Suarez, "Cyclostationary noise analysis of superregenerative oscillators," in *IEEE MTT-S Int. Microw. Symp. Dig.*, Jun. 2019, pp. 452–455, doi: 10.1109/MWSYM.2019.8701054.

[29] A. G. Armada, "Understanding the effects of phase noise in orthogonal frequency division multiplexing (OFDM)," *IEEE Trans. Broadcast.*, vol. 47, no. 2, pp. 153–159, Jun. 2001, doi: 10.1109/11.948268.

[30] E. S. Palamarchuk, "An analytic study of the Ornstein–Uhlenbeck process with time-varying coefficients in the modeling of anomalous diffusions," *Autom. Remote Control*, vol. 79, no. 2, pp. 289–299, Feb. 2018, doi: 10.1134/S000511791802008X.

[31] A. Demir, A. Mehrotra, and J. Roychowdhury, "Phase noise in oscillators: A unifying theory and numerical methods for characterization," *IEEE Trans. Circuits Syst. I, Fundam. Theory Appl.*, vol. 47, no. 5, pp. 655–674, May 2000.

[32] S. Sancho, A. Suarez, and F. Ramirez, "General phase-noise analysis from the variance of the phase deviation," *IEEE Trans. Microw. Theory Techn.*, vol. 61, no. 1, pp. 472–481, Jan. 2013, doi: 10.1109/TMTT.2012.2229713.

Sergio Sancho (Senior Member, IEEE) received the Licentiate degree in electronic physics from Basque Country University, Leioa, Spain, in 1997, and the Ph.D. degree in electronic engineering from the Department of Communications Engineering, University of Cantabria, Santander, Spain, in 2002.

At present, he works at the Department of Communications Engineering, University of Cantabria, as an Associate Professor. His research interests include the nonlinear analysis of microwave autonomous circuits, including stochastic, and phase-noise analysis.

Mabel Pontón (Member, IEEE) was born in Santander, Spain. She received the bachelor's degree in telecommunication engineering, the master's degree in information technologies and wireless communications systems, and the Ph.D. degree from the University of Cantabria, Santander, in 2004, 2008, and 2010, respectively.

In 2006, she joined the Department of Communications Engineering, University of Cantabria. From 2011 to 2013, she was with the Group of Electronic Design and Applications, Georgia Institute of Technology, Atlanta, GA, USA, as a Post-Doctoral Research Fellow. Her current research interests include the nonlinear analysis and simulation of radio frequency and microwave circuits, with an emphasis on phase-noise, stability, and bifurcation analysis of complex oscillator topologies.

Almudena Suárez (Fellow, IEEE) was born in Santander, Spain. She received the Licentiate and Ph.D. degrees in electronic physics from the University of Cantabria, Santander, in 1987 and 1992, respectively, and the Ph.D. degree in electronics from the University of Limoges, Limoges, France, in 1993.

She is currently a Full Professor at the University of Cantabria and the Head of the research group Microwave Engineering and Radiocommunication Systems. She was an IEEE Distinguished Microwave Lecturer from 2006 to 2008. She is the Publication Officer of EuMA since 2021. She has authored the book titled *Analysis and Design of Autonomous Microwave Circuits* (IEEE-Wiley, 2009) and co-authored the book titled *Stability Analysis of Nonlinear Microwave Circuits* (Artech House, 2003).

Dr. Suárez has been a Fellow member of the IEEE (for applications of stability analysis to the computer-aided design of microwave circuits) since 2012. She is a member of the TPCs of IEEE International Microwave Symposium and European Microwave Week. She was a member of the Board of Directors of European Microwave Association (EuMA) from 2012 to 2020. She received the Research Award of the Social Council of the University of Cantabria in 2021. She was the Coordinator of the Communications and Electronic Technology Area for the Spanish National Evaluation and Foresight Agency (ANEP) between 2009 and 2013. She was the Chair of the 2014 and 2015 editions of IEEE Topical Conference on RF/Microwave Power Amplifiers (PAWR), in Newport Beach and San Diego. She was the General TPC Chair of EuMW 2018. She has been the Chair of the IEEE Subcommittee for the Best paper Award in *IEEE Microwave Magazine* since 2017. She was the Editor-in-Chief of the *International Journal of Microwave and Wireless Technologies* from Cambridge University Press journals from 2013 to 2018. She is currently an Associate Editor for *IEEE Microwave Magazine* and the Editor-in-Chief of IEEE TRANSACTIONS ON MICROWAVE THEORY AND TECHNIQUES.